Transcritical real-fluid effects on dual-fuel combustion of methane and n-dodecane

Fathi, Mohamad; Roekaerts, Dirk; Hickel, Stefan

DOI
10.1016/j.jaecs.2025.100398

Publication date
2025

Document Version
Final published version

Published in
Applications in Energy and Combustion Science

Applications in Energy and Combustion Science 24 (2025) 100398

Contents lists available at ScienceDirect

Applications in Energy and Combustion Science

journal homepage: www.elsevier.com/locate/jaecs

Transcritical real-fluid effects on dual-fuel combustion of methane and n-dodecane☆

Mohamad Fathi, Dirk Roekaerts *, Stefan Hickel

Delft University of Technology, Mekelweg 5, Delft, 2628 CD, Netherlands

ARTICLE INFO

Keywords:
Transcritical
Jet flame
Combustion
Multiphase thermodynamics
Real-fluid
Dual fuel
Ignition delay
Radical pool
n-dodecane
Methane

ABSTRACT

A comprehensive set of accurate physical models and numerical simulation methods for transcritical dual fuel combustion systems is presented. The method combines multiphase real-fluid physical properties modeling, flamelet-based chemistry reduction, and large-eddy simulation (LES). It allows a fully integrated simulation of the multiphase region and the combustion zones in the turbulent flames. A central challenge in dual-fuel combustion applications is the successful ignition of low-reactivity ambient fuel by the high-reactivity pilot fuel jet. The interaction of the radical pools associated with both fuels is known to be an important characteristic. This study captures the evolution of this interaction across both the low-temperature combustion (LTC) and high-temperature combustion (HTC) regimes. Three cases are investigated, each involving the injection of an n-dodecane jet into a 6 MPa, 1000 K ambient. The cases differ only in ambient composition: (1) a single-fuel (SF) baseline case with a mixture of air and combustion products, and two dual-fuel (DF) cases with methane and a 90:10 (by volume) methane/ethane blend added to the ambient. Insights on ignition and flame structure are gained from homogeneous reactor simulations, transcritical counterflow diffusion flames, and LES. Combustion modes are defined by threshold levels of key species and temperature. The flame volume is subdivided according to the modes and for each mode the ignition delay and the temporal evolution of heat release rate (HRR) are obtained. The differences in the radical pools of SF and DF combustion are demonstrated. LTC ignition is shown to start in the multiphase region near the base of the jet. The high accuracy of the proposed methods provides a firm basis for modeling prospective dual-fuel systems using alternative fuels.

1. Introduction

Dual fuel combustion generally refers to the simultaneous use of two fuels, injected independently into a single combustor or engine. This can be done for various reasons, such as controlling radiative heat transfer or emissions; however, the special form considered here is specifically related to the design of internal combustion engines. It concerns the injection of a liquid diesel-like fuel into an ambient oxidizer mixed with a relatively low reactive fuel. Combustion of the jet fuel acts as a pilot flame to ignite the gaseous fuel. The ignition of the liquid fuel is often a two-step process, with the onset of low-temperature combustion (LTC) followed by the development of high-temperature combustion (HTC). This technique, referred to as diesel pilot ignition, is applied in many commercially available gas engines [1]. In recent years, significant progress has been made in understanding the autoignition mechanism in dual-fuel engine configurations, mostly using n-dodecane surrogate for diesel fuel and pure methane to represent natural gas. The dual fuel technique remains valuable while moving away from fossil fuels. Natural gas can be replaced by renewable fuels such as methanol [2], and fossil diesel can be blended with biodiesel or electrofuels [3]. Ghaderi Masouleh et al. [4] through homogeneous reactor models and premixed laminar flames studied the nature of dual fuel combustion as a function of the total fuel to air equivalence ratio and the molar ratio between the two fuels. They observed that while n-dodecane combustion enables a faster onset of methane combustion by rapidly forming radicals, at the same time, methane acts as a diluent and causes changes in the composition of the radical pool, significantly prolonging the pilot ignition delay time compared to a single-fuel n-dodecane case. Later, the phenomenon was confirmed in the context of large eddy simulations (LES) of spray jet flames. Representative references are given in Table 1. The cases studied in these works arise by direct extension of a single fuel benchmark n-dodecane injection known as ECN Spray A, characterized by parameters listed in Table 5. In liquid jet flames, the local composition of the reactant mixture is due to both phase change of the jet fuel and turbulent mixing. The

☆ This article is part of a Special issue entitled: 'Liquid fuel combustion' published in Applications in Energy and Combustion Science.

* Correspondence to: Faculty of Mechanical Engineering, TU Delft, Mekelweg 2, Delft, 2628 CD, Netherlands.
E-mail address: D.J.E.M.Roekaerts@tudelft.nl (D. Roekaerts).

https://doi.org/10.1016/j.jaecs.2025.100398
Received 20 July 2025; Received in revised form 12 September 2025; Accepted 25 September 2025
Available online 9 October 2025

combination of mixing and reaction leading to ignition is complex and difficult to model and simulate.

The focus of this work is on the additional complexity caused by the fact that the fuel jet is transcritical [5,6]. This situation arises when the combustion chamber pressure is greater than the critical pressure of the fuel but less than the maximum pressure for which phase equilibrium in a mixture of fuel and oxidizer can exist. In other words, the critical point of the fuel no longer represents the limit of the coexistence of liquid and vapor. Instead, two key boundaries emerge: the cricondenbar (maximum pressure allowing phase equilibrium) and the cricondentherm (maximum temperature allowing phase equilibrium). Unlike pure substances, mixtures can maintain liquid-vapor equilibrium above their critical temperature or pressure, as long as conditions remain below the limits set by cricondenbar and cricondentherm. This explains why variations of local composition can create two-phase regions even when the pressure and temperature of the system exceed the critical points of the pure components or their mixture. Both the real fluid effects and the possibility of co-existence of saturated liquid and vapor phases further complicate the modeling of transcritical fuel sprays. Such turbulent reacting sprays at transcritical pressures have drawn significant attention due to the complexity of the physical and numerical modeling [6].

These transcritical effects have rarely been considered in modeling studies of the single- and dual-fuel systems mentioned above. Instead, models developed for subcritical conditions have been used, assuming that a more refined treatment is not needed to reach an adequate model to predict the final spray flame accurately. Commonly used models combine submodels for fuel jet breakup providing a prediction of a droplet size distribution with models for momentum, heat and mass transfer between the phases. In Ref. [7], we have presented several novel physical and numerical models that improve the accuracy and computational efficiency of high-fidelity simulations of turbulent reacting and non-reacting multiphase flows at transcritical pressures. A comparison of the assumptions underlying different modeling approaches is presented in Section 2.1.

Our framework consists of a fully conservative formulation of the multi-component compressible Navier–Stokes equations with multiphase thermodynamics (MT) models and the adaptive local deconvolution method (ALDM) for the modeling of LES turbulence [8]. Improved accuracy compared to previous LES-MT simulations is provided by the RKPR EOS [9] for transcritical vaporization and real-fluid properties, and by fugacity-based finite-rate chemistry for combustion modeling. The computational cost is significantly reduced by a rapid VLE solver [10], which uses reduction methods for phase splitting calculations. In Ref. [11], we have applied the multiphase thermodynamics approach in simulations of transcritical counterflow diffusion flames and highlighted the essential role of accurate real-fluid models. Neglecting transcritical phase separation or using ideal gas assumptions was shown to lead to significant errors in transient ignition profiles. Finally, in Ref. [12] it is shown that using the real-fluid multiphase flamelet solver and the reduced chemistry description it provides, detailed analysis of chemical properties in turbulent transcritical flames is possible. The objective of this work is to demonstrate the predictive power of this approach in the simulation of dual-fuel systems.

The following objectives are proposed for the current investigation.

- Assess the performance of MT modeling in the prediction of dual-fuel transcritical spray flames.
- Demonstrate the interaction of jet fuel and ambient fuel in the early phases of ignition.
- Identify key factors that influence the different ignition behaviors in single-fuel and dual-fuel systems.

To realize these objectives, LES-MT simulations of three different cases were performed: the reference single fuel case (SF) and two dual fuel cases (DF_1 and DF_2), respectively with only methane and with a methane/ethane mixture in the ambient. The latter was added because it is closer to the real composition of natural gas than pure methane. The analysis addresses three different types of flow system: the constant volume homogeneous reactor, the counterflow diffusion flame and the three dimensional turbulent flame, each providing complementary insight.

Section 2 first presents the challenges to be addressed in multiphase modeling and reacting flow modeling and next addresses the question of what is the recommended approach to reveal the structure of an igniting dual-fuel flame. Section 3 provides a brief presentation of the models and numerical methods. Section 4 presents and discusses the simulation results. Conclusions are formulated in Section 5.

2. Challenges in modeling

2.1. Multiphase flow modeling

The atomization of the liquid jet in a surrounding gas phase and phase change from liquid to vapor involve the transfer of momentum, heat, and mass. In subcritical conditions, there is a clear separation between the saturation liquid and vapor phases. In transcritical conditions, a transition to a supercritical state without sharp interfaces can occur; however, states in the subcritical two-phase region may also be possible. Handling the simultaneous occurrence of these different states in multiphase flows is a challenge for modeling.

Many different computational methods have been developed for multiphase flows, and they can be subdivided into categories in different ways. Garcia-Villabla et al. [13] have presented a systematic review following a logical progression of numerical approaches and the underlying challenges they address. The approaches differ in the way in which an interface between different phases is described, conceptually and numerically. Either the aim is to represent a sharp interface (Volume-Of-Fluid (VOF) methods, level set methods, and front-tracking techniques), or to represent the interface using smoothing (diffuse interface methods). Other approaches use a statistical representation of the presence of the different phases (multi-fluid models, population balance models). Methods resolving the interface, either as sharp interphase or as diffuse interface, are suitable for the description of the first stages of breakup of a liquid jet. Once a subcritical jet has broken up in a collection of liquid fragments and finally in a dilute spray of spherical droplets, it becomes computationally not feasible to track the surface and it is more efficient to use the Lagrangian particle tracking (LPT) method, which can be connected to population balance models. In this method, model equations are used to describe the evolution of droplet properties (position, velocity, size, composition, etc.) over time [14,15]. In order to use the method, an initial droplet size distribution must be provided. To do so, a standard method is to use semi empirical methods for the primary and secondary breakup of a liquid jet. Recently, methods have been developed that combine interface resolving methods and LPT by introducing an algorithm for the conversion of liquid fragments smaller than a certain size to Lagrangian droplets based on well-defined criteria [16–18]. The LPT method has been widely used, also in simulations of transcritical sprays, in spite of the fact that it does not represent the possible loss of a sharp interface. Wehrfritz et al. [19] studied its submodel sensitivity and mesh sensitivity.

Another class of computational models assumes a diffuse vapor–liquid interface, neglects weak surface tension effects, and employs a cubic equation of state (EOS) to balance accuracy and computational cost. For example, Lacaze et al. [20] described how real-fluid thermodynamics influence liquid fuel injection under diesel engine conditions. While the single-phase dense gas (DG) approach is justifiable near supercritical conditions, its broader application to transcritical sprays is questionable, as ignoring phase separation can result in non-physical or ill-defined states when flows cross metastable boundaries [21].

A more robust alternative is the multiphase thermodynamics (MT) approach, which incorporates vapor–liquid equilibrium (VLE) calculations for multicomponent real-fluid mixtures using a consistent EOS.

In this method, rapid phase-splitting (flash) calculations determine the composition and quantity of coexisting saturated phases, from which thermo-transport properties are derived using appropriate mixing rules. When the mixture remains in a stable single-phase state, the MT yields results identical to those obtained by the DG method. For example, Gaballa et al. [22] proposed a fully compressible, multicomponent, two-phase real-fluid model (RFM) using a diffuse interface framework closed by a tabulated thermodynamic equilibrium method. Similarly, Jafari et al. [23] developed a tabulated multicomponent RFM within a fully compressible two-phase flow model employing a diffuse interface approach.

In summary, LPT neglects the non-ideal fluid effects, DG neglects the co-existence region effects, but MT takes into account both these effects. In the present work, we demonstrate and validate the application of the MT approach in the LES of transcritical jet flames.

2.2. Reacting flow modeling

High-fidelity simulations (DNS or LES) of turbulent combustion are computationally very demanding, and the addition of multiphase thermodynamics at transcritical conditions enlarges this problem even more. Single-phase turbulent combustion simulations have benefited from cost savings by using reduced chemical mechanisms and flamelet-based models [24]. For the fuels studied in this work, detailed mechanisms and reduced mechanisms with different levels of reduction are available. However, reduced mechanisms have a limited validity range. The range can be quantified, based on assumptions made in the derivation and specific validation tests, such as the prediction of the ignition delay time or the flame propagation speed. In the case of the igniting transcritical jet flame, the accurate representation of the ignition delay time as a function of mixture composition and initial temperature is a must and should be tested a priori. In LES-DG methods direct chemistry integration using highly-reduced reaction mechanisms has been used as part of studies on the impact of the real-fluid environment and low-temperature chemistry [25–27]. Flamelet based models lead to a reduced representation based on assumptions on the local flame structure. In LES-LPT methods, non-premixed igniting flamelet models are typically considered due to the fact that the main combustion mode in liquid fuel spray flame engines is non-premixed and autoignition is inherently transient [28–30]. Based on detailed chemistry simulations of laminar counterflow diffusion flames (CDF), a very low-dimensional subspace (manifold) is obtained, with typically mixture fraction and progress variable as independent composition variables, providing the reduced representation (tabulated chemistry) used in the turbulent flame [31].

Our work, using LES-MT, started by using an optimized two-step reaction mechanism developed by Hakim et al. [7,32]. In subsequent work, we have used a new flamelet generated manifold method. First, a method for the computation of igniting CDFs using multiphase thermodynamics was developed [11]. The manifolds generated by this method were then applied in simulations of transcritical jet flames of n-dodecane, OME_3 and a mixture of both [12] using a combined mechanism of Lapointe et al. [33] and Lin et al. [34]. The proposed transcritical manifold approach represents both multiphase thermodynamics and real-fluid chemistry and, by construction, provides direct insight into the distance between the multiphase region and the region where the first ignition occurs. It is explained further in Section 3.2.2. The use of igniting non-premixed flamelets to construct the FGM has limitations. Depending on the conditions, other modes of combustion may occur. For example, it has been observed that in dual fuel cases with methanol as secondary fuel, the lean ambient mixture can ignite by autoignition leading to premixed flame propagation [2]. In such a situation, a more general approach that includes multiple flame structures would be needed.

A final modeling problem to be addressed is the representation of the influence of subgrid scale (SGS) fluctuations on the resolved chemical source term. The simplest approach, also followed here, is to neglect this by computing the resolved source term by substituting the resolved composition variables (concentrations and temperature) in the laminar rate expressions often called the well-stirred reactor (WSR) model in literature. Hadadpour et al. [35] presented an overview table of the TCI closure modeling used in 21 LES studies of ECN spray A and spray H flames, also listing the minimum cell size. It shows that a wide range of models has been used, divided as follows: WSR (8), Partially Stirred Reactor (PaSR) (4), Conditional Moment Closure (CMC)(1), Flamelet (1), FGM (3) and Transported PDF (4). Because these studies also differ in the selected chemical mechanism a general conclusion of the relative importance of TCI model cannot be drawn. The finest grids have been used in combination with WSR with minimum cell size $62.5\,\mu m$, while other approaches use grids up to a factor of eight times larger. This agrees with the fact that in explicit LES modeling, where the LES filtering is controlled by the computational mesh, the accuracy of the WSR approach is expected to increase with grid refinement, because the assumption of homogeneity becomes more plausible. This is further elaborated in Section 3.2.3.

2.3. Dual-fuel combustion

In the dual-fuel systems considered in this work, the diesel-like jet combustion acts as a pilot for the ignition of a gaseous fuel mixed with the oxidizer. The challenge in designing the system is to determine the optimal amount and injection time of the liquid depending on the composition of the ambient. The modeling challenge concerns the integration of models for the different fuels in a model describing the coupling between their combined combustion in one oxidizer. The final comprehensive model should be accurate without needing parameter tuning.

In the recent literature, considerable attention has been paid to the case of a jet of n-dodecane in a homogeneous mixture containing methane. This is a direct generalization of the base case ECN Spray A where no methane is present in the ambient. Several cases differing in ambient temperature and methane concentration have been studied. An overview of the experimental and modeling results until 2018 has been provided by Kahila et al. [36]. Experimental studies have revealed that the ignition of a diesel spray is retarded when the ambient air contains methane, compared to ignition in pure air, demonstrating a coupling between the combustion of both fuels. The pilot ignition was observed to be a volumetric process within the spray envelope, showing a linear relationship between ignition delay time (IDT) and methane concentration. Both stages of ignition were delayed, but the time shift between LTC and HTC was found to be almost constant and independent of the methane concentration. The retarding influence of methane was observed to be higher at lower ambient oxidizer temperature.

Some key aspects of previous LES modeling studies and the present work are listed in Table 1. These studies not only present LES results, but also analysis using homogeneous reactor models and/or laminar flamelets, providing useful information on dependence of ignition delay time on initial composition and temperature and sensitivity to the chemical model. All cited references also include model validation for ECN Spray A, with ambient temperature $900\,K$, either in the cited reference or in previous work, for example Kahila et al. [1]. The studies cited in Table 1 have been carried out using LES with implicit closure (ILES, ALDM) or a dynamic structure model on a mesh with several steps of grid refinement with similar total number of cells. See Moser et al. [37] for a comparative analysis of the qualities of different LES formulations. The studies listed in the Table describe the injection of liquid fuel as a spray of evaporating droplets (LPT) embedded in ideal gas, with the exception of this work, which uses the MT approach explained in Section 2.1. The tabulation method used by Bao et al. [38] is based on gaseous CDFs, using scalar dissipation rate as an extra independent scalar in addition to the mixture fraction and the progress

Table 1
Selected studies on dual fuel combustion of transcritical n-dodecane liquid jet in an ambient containing methane at temperature T and equivalence ratio of the ambient mixture ϕ. The mole fraction of oxygen in the ambient in all cases is set to 15%. References for the chemical mechanisms: Yao [39], Ranzi [40], Lapointe [33]. Tab. refers to chemistry tabulation via flamelet methods.

Reference	Ambient T [K]	Ambient ϕ	Chem. Mech.	LES
Kahila et al. [36]	900	0.5	Yao	ILES
Tekgü et al. [41]	850/900/1000	0.5	Yao	ILES
Bao et al. [38]	900	0.25/0.5/0.75	Yao + Tab.	Dynamic
Karimkashi et al. [2]	900/950/1000	0.5	Ranzi	ILES
Wei et al. [42]	900	0.2/0.4/0.6	Yao	Dynamic
Gadalla et al. [43]	900	0.5	Yao	ILES
This work	1000	0.5	Lapointe + Tab.	ALDM

variable [29]. The tabulation method used in the present work is based on transcritical flamelets, as explained in Section 3.2.2.

Kahila et al. [36] demonstrated the inhibition effect of methane on the ignition of n-dodecane in LES and also showed using a reaction rate sensitivity analysis in representative mixtures that ambient methane influences the early decomposition of n-dodecane mainly by consuming the OH radical and forming methyl radicals that activate other inhibiting reactions. They noted that these results indicate that the influence of methane on the early decomposition of long hydrocarbons should be considered in detail when working with dual fuel applications. Tekgül et al. [41,44] and Karimkashi et al. [2] studied the sensitivity of ignition to ambient temperature. Bao et al. [38] and Wei et al. [42] studied the impact of ambient methane concentration on ignition and flame structure. Wei et al. [42] performed extensive kinetic analysis of the reaction pathways involved in the inhibition effects. Gadalla et al. [43] went beyond LES by introducing an embedded DNS of ignition kernel evolution and flame initiation. Their analysis addressed the reaction front displacement speed, the energy transport budget, and chemical explosive mode analysis.

This summary leads to the conclusion that the complex chemical kinetics involved in dual fuel combustion is an extraordinary challenge for turbulent reacting flow modeling. Here, by making use of the MT approach, and an appropriate chemical mechanism, the initial composition profiles arising in the mixing region of jet and ambient, are accurately represented. This approach is needed to correctly predict the low temperature combustion modes, discussed in the next Section.

2.4. Combustion modes

Interpretation of LES predictions of a complex multispecies and multistep ignition process is only possible when key ignition characteristics have already been identified. These can be done via preliminary *kinetics only* simulations, revealing important chemical pathways and characteristic ignition delay times. Threshold values of specific species concentrations and temperature can be used as markers of phases of ignition, called modes [2,45]. Once the modes are defined, they can be used to find a structure in the computed flames.

In the presence of multistep kinetics, ignition is the result of a series of steps. For the class of liquid fuels considered, both LTC and HTC have to be considered. For LTC the concentration of hydrogen peroxide, H_2O_2, and for HTC the concentration of hydroxyl radical, OH, have been selected as key ignition indicators. To represent the evolution towards LTC with higher precision, it is also important to consider the first product of oxidation. In some previous studies of the n-dodecane flame, $C_{12}H_{25}O_2$, more generally denoted RO_2, where R denotes the fuel radical, has been selected [45]. In this work, the chemical mechanism of Lapointe et al. [33] for alkanes C_nH_{2n+2} is used. In the derivation from a more detailed mechanism, RO_2 has been eliminated by making the combination of two oxidation reactions, passing the role of the first product of oxidation explicitly present in the mechanism from RO_2 to a ketohydroperoxide species ($C_{n-1}H_{2n-1}OOHCO$), denoted KET_1, for the case $n = 12$ in this paper. The first reaction step in the reduced mechanism is then $R+2O_2 \rightarrow KET_1 + OH$. Further information on the mechanism is given in Section 3.2.1. The objective this work is to demonstrate the strength and weakness of the use of the Lapointe et al. mechanism in prediction of transcritical flow, including comparison with literature results using other mechanisms.

Table 2
Criteria defining combustion modes.

Low-temperature combustion modes ($T < 1150$ K):	
LTC	$(KET_1 \geq 10^{-7}) \cap (H_2O_2 < 10^{-4})$
LTC-late	$(KET_1 \geq 10^{-5}) \cap (H_2O_2 \geq 10^{-4})$
pre-HTC	$(KET_1 < 10^{-5}) \cap (H_2O_2 \geq 10^{-4})$
High-temperature combustion modes ($T \geq 1150$ K):	
HTC pre-ign.	$OH < 10^{-5}$
HTC	$OH \geq 10^{-5}$

Before KET_1 can be produced by chemical reaction in the gaseous phase, mixing of evaporated fuel and oxidizer must have occurred. The detailed representation of the multiphase thermodynamics used in this work provides an accurate description of the initial mixture. Possible combustion modes are defined by setting thresholds of mass fractions of key species and the temperature [45]. The definitions are summarized in Table 2, including the selected threshold values. The LTC modes by definition are the same for the single-phase region and the two-phase region. A liquid phase is not present above the threshold temperature for HTC.

After mixing of fuel vapor and oxidizer, KET_1 can result from chemical reactions, and when it reaches a threshold value the LTC regime is entered. The LTC regime is divided in three parts LTC, LTC-late and pre-HTC. In the LTC regime where heat release rate (HRR) is primarily originating from early-stage n-dodecane decomposition, KET_1 is above threshold but H_2O_2 is below threshold, in the LTC-late regime where production of LTC-related species accumulate (e.g. KET_1, H_2O_2, CH_3, and HO_2), KET_1 and H_2O_2 both are above their threshold values. The disappearance of the long-chain hydrocarbon radicals such as KET_1 from the mixture is taken as a sign that the radical pool has shifted to conditions favorable for HTC. Hence the pre-HTC regime is defined by KET_1 being below threshold while H_2O_2 is still above threshold. This regime continues until the temperature reaches a threshold value of 1150 K.

It should be pointed out that the name of the modes used in literature is not universal. The mode names LTC and LTC-late, introduced by Kahila et al. [45] and used here, correspond to Early LTC and LTC by Karimkashi et al. [2]. Furthermore, the list of combustion modes defined in Table 2 does not cover possible gaseous states with negligible HRR, in which KET_1 and H_2O_2 both are below their threshold values. It also does not cover the exceptional case that H_2O_2 has decreased below threshold for pre-HTC while temperature is still lower than the threshold for HTC modes. The occurrence of these states is documented in Section 4.3.4.

The partitioning of flames according to the modes can be used in several ways. The manifold used in the tabulated chemistry approach can be partitioned according to the modes realized locally at fixed mixture fraction and progress variable. The changes in the thermochemical composition in the turbulent flame can be revealed in the spatial structure, or in the structure in composition space, the location on the manifold. Identification of these modes makes it possible to reveal important overall characteristics of the flame.

3. Models and numerical methods

In this section we give a summary of the models and numerical methods. More information can be found in our previous articles [7,11,12,46].

Table 3
Real-fluid transcritical properties modeling described in [11].

Property class	Property	Basic model	Specific model
Thermodynamic	Volumetric EOS	Cubic	RKPR of Cismoni and Mollerup
	Caloric EOS	Departure formalism	NASA polynomials
	Multiphase EOS	Including phase splitting	PT-flash
Transport	Viscosity and conductivity	Chung et al.	Effective medium theory EMT
	Diffusion mass flux	Dixon-Lewis formulation	Naud and Arias-Zugasti approximation
	Binary diffusion coeff.	Chapman-Enskog theory	Real fluid correction factor
Chemical	Rate expression	Law of mass action	Fugacity based concentration

3.1. Multiphase thermo-transport properties

The presence of a multiphase region in the transcritical jet flame requires considerable extension of the models for thermodynamics and transport compared to those under subcritical conditions. The list of properties for which model extensions are required, with an indication of the basic models and refinements, is given in Table 3. The thermodynamic properties of the working fluid are computed by solving suitable volumetric and caloric state equations combined with phase-splitting equations. A cubic EOS is selected as a practical compromise among accuracy, complexity, and computational cost:

$$p = \mathcal{R}T/(\bar{\vartheta} - b) - a/[(\bar{\vartheta} + \delta_1 b)(\bar{\vartheta} + \delta_2 b)]. \tag{1}$$

The symbol $\mathcal{R}$ represents the universal gas constant and $\bar{\vartheta} \equiv W/\rho$ is the molar specific volume of the mixture in which W and ρ are mean molecular weight and density of the mixture. δ_1 and δ_2 as well as a and b are four parameters of the cubic EOSs in general. For mixtures, these parameters can be determined using the van der Waals mixing rule. We consider RKPR to be the leading three-parameter cubic EOS, with $\delta_2 = (1 - \delta_1)/(1 + \delta_1)$, and used it in our study. The caloric EOS can be obtained by employing the departure function formalism consistent with the utilized volumetric EOS as follows:

$$\bar{e} = \sum_{i=1}^{N} X_i \bar{h}_i^\circ - \mathcal{R}T + (a - T\partial a/\partial T)/[(\delta_2 - \delta_1)b] \times \ln[(\bar{\vartheta} + \delta_1 b)/(\bar{\vartheta} + \delta_2 b)], \tag{2}$$

with $\bar{e} \equiv e/W$ being the molar specific internal energy. The first two terms represent the mixture's absolute internal energy at the actual temperature under standard pressure, while the last term reflects the internal energy change along an isothermal path from the reference to the actual pressure. X_i denotes mole fraction of species i. The molar specific enthalpy $\bar{h}_i^\circ$ of pure species i at the standard pressure (including the formation enthalpy) is calculated using NASA polynomials. In two-phase regions, the molar composition of the liquid and vapor phases is set using vapor–liquid equilibrium calculations by equality of the fugacity of species in the liquid and vapor with two extra constraints that set the type of the problem. In solving the fully conservative compressible Navier–Stokes equations, isoenergetic-isochoric phase-splitting or UV-flash calculations are necessary. The two additional constraints for these calculations are

$$\bar{\vartheta} = (1 - \theta)\bar{\vartheta}^L + \theta\bar{\vartheta}^V, \tag{3}$$

$$\bar{e} = (1 - \theta)\bar{e}^L + \theta\bar{e}^V. \tag{4}$$

Here θ represents the molar ratio of vapor to total (vapor and liquid). The transport properties of the working fluid are modeled using high-pressure correction methods with appropriate structural mixing rules in the co-existence regime [46]. The effective medium theory (EMT) used to evaluate the effective viscosity and conductivity of the mixture in the presence of phase splitting assumes a random spatial distribution of the two phases [47]. Real-fluid effects on the diffusion driving force are quantified via the thermodynamic correction factor with a proposed extension to the multiphase transcritical regime. The finite-rate chemistry model includes real-fluid high-pressure effects in reaction source terms via the fugacity of the species.

Table 4
Size characteristics of chemical mechanisms.

Name	# Species	# Reac
Narayanaswamy [48]	255	1512
Ranzi [40] (POLIMI reduced)	130	2323
Lapointe [33]	65	363
Yao [39]	54	269

The models are described in detail in Ref. [11], including a comparative analysis with simpler models. The results obtained for homogeneous reactors and laminar flames demonstrate the need for these accurate models and their impact on the predicted ignition behavior of transcritical flames.

3.2. Combustion modeling

3.2.1. Reaction mechanism

An essential factor for selecting a chemical mechanism is its ability to give an accurate prediction of the ignition process. Both LTC and HTC regimes and the negative temperature coefficient (NTC) regime should be accurately captured for both the SF and DF cases.

In this work the mechanism proposed by Lapointe et al. [33] is used. It is the result of a general hybrid approach to develop reduced kinetic models for complex engine relevant fuels. This strategy offers a good balance between accuracy and computational efficiency. The resulting mechanism is composed of a small fuel-dependent submechanism of ten reactions and a fuel-independent core submechanism obtained from the Narayasmany mechanism [48].

To support the discussion of results in Section 4.1, here some information on the key properties of the Lapointe mechanism is provided. Fuel breakdown and radical oxidation are modeled through the following key reactions:

$$\mathrm{F + X \rightarrow R + XH},$$

$$\mathrm{R + 2O_2 \leftrightarrow KET_1 + OH},$$

$$\mathrm{KET_1 \rightarrow} \textit{ core chemistry species } \mathrm{+ OH}.$$

These reactions are complemented by simplified high-temperature fuel pyrolysis pathways:

$$\mathrm{F \rightarrow} \textit{ core chemistry species},$$

$$\mathrm{R \rightarrow} \textit{ core chemistry species}.$$

Here F in our case is n-dodecane and R represents the fuel radical. X denotes a species among H, O, OH, HO_2, O_2, and CH_3O_2, KET_1 represents a ketohydroperoxide species and *core chemistry species* refers to the fuel-independent base mechanism. Multiple isomers are considered in the mechanism.

Table 4 compares key size parameters of the Lapointe mechanism with those of other mechanisms used in previous DF studies (see also Table 1). A more detailed comparison can be found in Refs. [4,42]. Kilic et al. [49] compared the performance of reduced n-dodecane mechanisms of Yao and Lapointe. Both mechanisms reproduced the ignition behavior reasonably well in pure diesel configurations, with the Lapointe mechanism having relatively better performance. However,

their LES results showed that Yao may not be suitable for dual fuel applications at low ambient temperature (750 K). Our recent work [11] has also shown that the Lapointe mechanism can accurately capture ignition delays under transcritical real-gas conditions, which further justify its use for the present simulations.

3.2.2. Counterflow diffusion flames based manifold

In the tabulated chemistry approach to turbulent flame modeling the evolution in thermochemical state space is described as evolution in a lower-dimensional manifold. In the FGM approach used here, the manifold consists of states reached in representative laminar flames. Because the ambient mixture is slow to ignite, the jet is expected to burn in non-premixed mode. For transcritical pressures, the configuration involves the injection of a liquid- or liquid-like fuel and a gaseous- or gaseous-like oxidizer in opposite directions, resulting in the formation of a reaction zone near the stagnation plane. The governing equations are reduced to a quasi-one-dimensional form along the axis of symmetry. Moreover, since ignition is the key problem that should be represented well, a transient igniting flame is selected as the basis for the table. The theoretical and numerical details of the transcritical CDF approach are described in Ref. [11]. The strain rate applied on the CDF was set to 100 s^{-1}, based on a preliminary study on the dependence of IDT on strain rate [12]. The generalized approach using strain rate as an additional independent variable has been used in the context of transcritical spray flames by Bao et al. [29] and Haspel et al. [50]. Considering that ignition is found to occur fastest in a small range of strain rates, and the additional cost of adding an extra independent variable, here we choose to work with one carefully selected strain rate.

A mixture fraction $\mathcal{Z}$ and a progress variable C are used as independent variables to tabulate all thermochemical states reached, including also the chemical source term of the progress variable. They are both obtained by solving additional transport equations. The diffusion of $\mathcal{Z}$ is described by assuming the Lewis number $Le_{\mathcal{Z}} = 1$. The relation to a definition of mixture fraction based on element mass fractions is discussed in Section 4.2. The progress variable is initialized based on O_2 and normalized to be 0 in the pure mixing state and to be maximal when all O_2 are consumed:

$$C = Y_{N_2}(Y^0_{O_2}/Y^0_{N_2}) - Y_{O_2}. \tag{5}$$

Here, $Y^0_{O_2}$ and $Y^0_{N_2}$ are values dependent on $\mathcal{Z}$ on the mixing line. During flamelet computations, the source term in the progress variable transport equation is computed from this definition and the source term of O_2 and N_2[11]. The diffusion of C is described assuming $Le_C = 2$. This implies that the value of C obtained by the transport equation differs from the value obtained by substituting the solution of the species mass fraction equations in the definition (5). This is not a problem since C is an extra auxiliary variable, used as a coordinate on the FGM, connecting flamelet data to thermochemical properties in the turbulent flow simulation. The relatively high value $Le_C = 2$ is not crucial, but it is convenient because it leads to a smooth representation of the reaction zone as a function of the manifold coordinates.

For each of the cases described in Table 6 a separate look-up table is generated with the size of (256×1024) points, uniformly distributed in the mixture fraction and the progress variable directions, and taking into account the boundary conditions of the case.

3.2.3. Large eddy simulation model

We use the LES-MT method presented in [7]. The reacting multiphase compressible Navier–Stokes equations are solved using the adaptive local deconvolution method (ALDM) for LES turbulence modeling [8]. This is combined with the multiphase models described in 3.1 and the tabulated chemistry approach described in 3.2.2.

The governing equations for mass, momentum, and total internal energy for a single-fluid multicomponent compressible flow are

$$\partial_t \rho + \boldsymbol{\nabla} \cdot (\rho \mathbf{u}) = 0, \tag{6}$$

$$\partial_t \rho \mathbf{u} + \boldsymbol{\nabla} \cdot (\rho \mathbf{u}\mathbf{u} + p\mathbf{I}) = \boldsymbol{\nabla} \cdot \left[\mu \left(\boldsymbol{\nabla}\mathbf{u} + (\boldsymbol{\nabla}\mathbf{u})^T\right) - 2/3\mu\,(\boldsymbol{\nabla} \cdot \mathbf{u})\,\mathbf{I}\right], \tag{7}$$

$$\partial_t \rho e_t + \boldsymbol{\nabla} \cdot [(\rho e_t + p)\mathbf{u}] = \boldsymbol{\nabla} \cdot (\mathbf{u} \cdot \boldsymbol{\tau} + \lambda \nabla T). \tag{8}$$

in which ρ is the density, $\mathbf{u}$ is the velocity vector, p is the thermodynamic pressure, T is the temperature and e_t is the total specific internal energy, which includes both the internal energy e and the kinetic energy. The energy conservation equation excludes a source term, because energy is calculated using the heat of formation. The thermal conductivity and molecular viscosity are indicated by λ and μ. To determine the thermodynamic state of the working fluid, we need the internal energy, density, and composition of the mixture. The composition is obtained from the look-up table based on the mixture fraction ($\mathcal{Z}$) and the progress variable (C) calculated using the following equations:

$$\partial_t \rho \mathcal{Z} + \boldsymbol{\nabla} \cdot (\rho \mathbf{u} \mathcal{Z}) = \boldsymbol{\nabla} \cdot (\lambda / c_p \nabla \mathcal{Z})/\mathrm{Le}_{\mathcal{Z}}, \tag{9}$$

$$\partial_t \rho C + \boldsymbol{\nabla} \cdot (\rho \mathbf{u} C) = \boldsymbol{\nabla} \cdot (\lambda / c_p \nabla C)/\mathrm{Le}_C + \dot{\omega}_C. \tag{10}$$

where, c_p is the heat capacity of the mixture. $\dot{\omega}_C$ is the source term of the progress variable, obtained from the look-up table. $\mathrm{Le}_{\mathcal{Z}} = 1$ and $\mathrm{Le}_C = 2$, as has been used in the auxiliary equation solved together with the species equations during the computation of the flamelet, providing full consistency [51].

The source term of the resolved progress variable is computed using the WSR model, neglecting subgrid scale composition fluctuations. As mentioned in Section 3.2 this can be an acceptable approximation when the mesh is sufficiently fine. In the LES reported here, the minimum cell size is 10.25 μm, significantly smaller than in all previous works cited in Ref. [35] and also smaller than the typical size of the reaction zones in the transcritical flamelets [11]. Therefore, the assumption that TCI has very small impact can be used. Pei et al. [52], in a detailed RANS analysis of the flame structure of Spray A, have proposed a quantitative criterion to decide whether an LES filter is fine enough to neglect TCI, namely the Damköhler number based on the smallest resolved scales $Da_3 > 1$. Since flow time scales are becoming larger with increasing axial distance, whereas the chemical time scales are becoming shorter with temperature, this criterion is local. Further work on the use of this criterion would be of interest.

3.3. Validation test cases

The objective of this work is to extend the application of the multiphase thermodynamics approach from single fuel to dual fuel systems and to evaluate its performance in comparison with other approaches. First, we present the motivation for the selected test cases and their specification.

The most relevant observations on the differences between the two approaches can be expected when the ignition occurs close to the two-phase region. Since it was observed that the IDT, and also the distance from injector to the ignition location, is larger in the dual fuel case but less so when the temperature of the ambient is higher, in this study we select an ambient temperature of 1000 K instead of the standard 900 K of the Spray A case. The results obtained for this condition can be compared with the LPT based studies reported by Tekgül et al. [41,44], Bao et al. [38], Karimkashi et al. [2], and Gadalla et al. [43]. See Table 1 for a summary of the models used in these works.

Three cases are studied. They all have the same injection of n-dodecane. In the first case, there is no second fuel present. In the two other cases the fuel in the ambient gas respectively is methane, and a mixture of methane and ethane. The latter is selected as a simple representation of the composition of liquefied natural gas (LNG). With no hydrocarbons higher than ethane present, it can be described by the Lapointe chemical mechanism. Here we set the molar ratio of the two components to CH_4:C_2H_6 = 90:10. The reactivity of the mixture and resistance to knock is increasing with decreasing methane/ethane

Table 5
Liquid fuel injection parameters.

Fuel	n-dodecane
Nominal nozzle diameter [μm]	90
Fuel temperature [K]	363
Injection pressure [MPa]	150
Injection duration	Continuous

Table 6
Ambient conditions in different testcases: single fuel (SF) with inert ambient; dual-fuel cases of (DF_1) with CH_4 and (DF_2) with CH_4 and C_2H_6 in their ambient oxidizer.

Acronym	SF	DF_1	DF_2
Temperature [K]	1000	1000	1000
Pressure [MPa]	6	6	6
Density [kg/m^3]	20.87	20.43	20.48
O_2 [% mol]	15	15	15
CO_2 [% mol]	6.23	5.95	5.97
H_2O [% mol]	3.62	3.46	3.47
N_2 [% mol]	75.15	71.83	72.06
CH_4 [% mol]	0	3.75	3.14
C_2H_6 [% mol]	0	0	0.35
ϕ_{CH_4}	0.0	0.5	0.5
Z_{st}	0.0451	0.0234	0.0233

ratio. This is commonly expressed by the methane number MN [26]. According to the Kubesh et al. correlation, the selected blend has MN = 85.5 which is above the minimum value required for gas engines [26]. The injection parameters, the molar composition of the ambient and the physical parameters of the three cases are listed in Table 6. The composition is uniquely determined by the imposed O_2 concentration and the equivalence ratio. The stoichiometric value of the mixture fraction according to the Bilger definition, Z_{st}, corresponds to the optimal condition to reach complete combustion and higher peak temperature, but first ignition may occur on either side of the stoichiometric value, at the most reactor mixture fraction value Z_{mr}.

4. Results and discussion

Previous studies have shown that the presence of methane in the ambient environment has an inhibiting effect on ignition. This effect becomes more pronounced with increasing methane concentration and decreases at higher ambient temperatures. In this section, we examine how this inhibitory effect manifests itself in simulations that incorporate multiphase thermodynamics. Furthermore, we analyze the sensitivity of this inhibition to the composition of the ambient fuel mixture, comparing pure methane with a methane/ethane mixture. First, we investigate the ignition process using homogeneous reactor simulations to analyze the sequential steps leading to ignition. Next, we use laminar counterflow diffusion flame configurations to identify the locations of different combustion modes in the composition space. Finally, large eddy simulations (LES) of turbulent flames are used to examine the transient development of these modes and to determine the resulting flame structure.

4.1. Homogeneous reactor simulation

Homogeneous reactor simulations have been used in the literature both to study the characteristics of the first steps to LTC and the chemical sensitivities of the time to reach HTC. Ghaderi Masouleh et al. [4] have made a comparative analysis of results for a range of dual fuel cases with different n-dodecane to methane ratios and different equivalence ratios, using the Ranzi (POLIMI) reduced mechanism [53]. They distinguished three steps: decomposition of n-dodecane (I), introduction of reactive radicals in the system (II), and ignition of the mixture (III). Methane ignites faster than in the absence of n-dodecane because of the presence of radicals coming from steps I and II, but on the other hand, both as diluent and by the role played by methane decomposition products in radical chemistry, full ignition of the jet flame is slower than in the absence of methane. Kahila et al. [36] studied the sensitivity of ignition delay time (IDT), the time required to reach the maximal temperature increase rate, to reaction rates using homogeneous reactor computations for both SF and DF_1 (but at ambient temperature 900 K), for two reduced mechanisms of Yao et al. [39] and Ranzi et al. [40]. They considered three initial mixture compositions, namely mixtures with the overall fuel to ambient equivalence ratios $\phi = 0.5$ and $\phi = 1.0$ and mixture at the most reactive mixture fraction $\phi_{mr} = \left[Z_{mr}\left(1 - Z_{st}\right)\right] / \left[Z_{st}\left(1 - Z_{mr}\right)\right]$. They observed that addition of CH_4 in the ambient mixture has an impact on the chemical pathways and production and consumption rates of intermediate species such as OH, CH_3, HO_2, and early decomposition products of n-dodecane such as RO_2. Differences in ignition delay times were observed between the Yao mechanism and the Ranzi (POLIMI) mechanism.

Fig. 1 gives a comparative analysis of the predictions of the inhibition effect by the three mechanisms: Lapointe, Ranzi, and Yao. The figure shows the predicted time evolution of a homogeneous reactor for n-dodecane fuel premixed with oxidizers DF_1 and DF_2 at three values of the equivalence ratio, namely 0.5, 1 and 2. The origin of the time axis for each graph is set to the ignition delay time of the corresponding SF oxidizer case: t_0 = IDT(SF), which was computed separately. In this way, the time shift between cases directly shows the inhibition effect. The Lapointe mechanism predicts a lower increase of ignition delay compared to the SF case than the mechanisms of Ranzi and Yao. The difference between the DF_1 and DF_2 cases is very small. The result of the Narayanaswamy mechanism has also been added. Its results coincide with the Lapointe result. The difference between both mechanisms is that Narayanaswamy is a skeletal mechanism derived from the LLNL detailed mechanism, and the Lapointe mechanism is a hybrid mechanism combining an innovative fuel-specific part and a non-fuel-specific part derived from the LLNL mechanism. It shows that the difference with Ranzi and Yao is not due to the fuel-specific part of Lapointe, but due to the core mechanism that it has in common with Narayanaswamy. More detailed comparison of results on the basis of a single equivalence ratio and a single initial temperature is not meaningful, because the equivalence ratio of the fastest ignition is known to depend on the mechanism [36]. Tekgül et al. [41] have presented a more extensive comparison of IDTs predicted by different mechanisms, including the dependence on initial temperature and equivalence ratio. Extending their analysis by including the Lapointe mechanism can provide further insight.

Next, we present the species concentration evolution predicted by the Lapointe mechanism. Fig. 2 shows transient profiles of key species involved in the first ignition steps for the case $\phi = 1$. In the SF case, a rapid increase in radicals, including KET_1 (phase II) is observed after less than 0.1 ms. In the DF cases, the rise comes later and is slower. The difference between DF_1 and DF_2 is not large. In agreement with the result of Fig. 1 that the delay of full ignition of the DF cases compared to the SF case is about 0.3 ms at $\phi = 1$, Fig. 2 shows that right from the start the DF cases show a slower development of the radical pool.

According to Wei et al. [42] the inhibition of ignition by presence of methane arises because methane and n-dodecane combustion are in competition for OH radicals. Ghaderi Masouleh et al. [4] have suggested that the mere presence of the light molecule methane could inhibit n-dodecane decomposition by its influence on third-body collisions that play a role in the fuel decomposition reaction rate. The early decomposition is confirmed by the results shown in Fig. 2. The decomposition of n-dodecane starts earlier than the rise of radicals. However, the radical pool has increased significantly before the n-dodecane is depleted. During the build-up of the radical pool, only a minor fraction of the methane has decomposed. The small spikes in the methane and ethane profiles correspond to their formation from n-dodecane decomposition products. All this is in line with the conclusion of Kahila et al. [36] that the influence of methane on the early decomposition of long hydrocarbons should be considered in detail when working with DF applications.

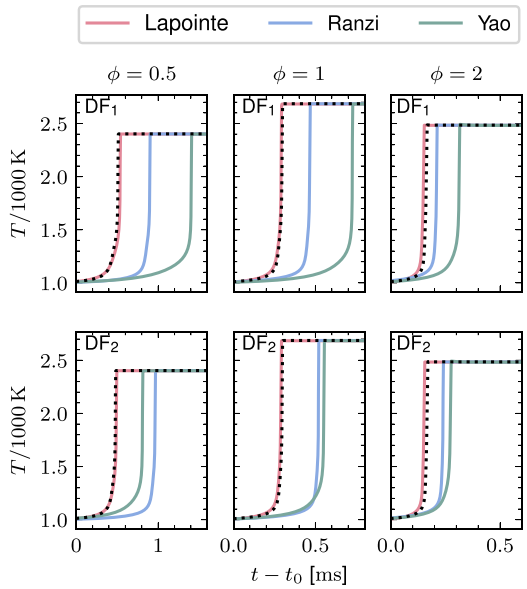

Fig. 1. 0D reactor predictions of the increase, compared to the corresponding single fuel case, of ignition delay time. Results for dual fuel cases DF_1 and DF_2, for Lapointe, Ranzi and Yao mechanisms, in lean, stoichiometric, and rich mixtures. Dotted lines represent the result of mechanism of Narayanaswamy et al. [48]. The initial temperature and pressure are set to 1000 K and 6 MPa.

4.2. Flamelet generated manifold simulation

4.2.1. Counterflow diffusion flame simulation

The following procedure was followed to compute the transient flamelet. Dirichlet boundary conditions are applied at both inlets for temperature, species mass fractions, mixture fraction, and progress variable. The progress variable source term is also set to zero at both inlets. The simulation proceeds in two stages: First, a steady counterflow solution is obtained with the chemistry turned off; then, the reactions are enabled, and the transition simulation continues in steady state. The resulting states from the second stage define the tabulated chemistry manifold. A strain rate of $100\,s^{-1}$ is imposed on the oxidizer side, while a Neumann boundary condition is applied on the fuel side. The initial stretch rate profile is computed from the strain rate and the local density [11].

The results of the transient flamelet calculation can be displayed as a function of the mixture fraction obtained from Eq. (9). This mixture fraction is assumed to have $Le_{\mathcal{Z}} = 1$ and, although it is a very convenient variable as a tabulation coordinate, in its description of mixing, it does not keep track of the effects of differential diffusion. As a result, the location of the stoichiometric mixture will be shifted in mixture fraction space compared to the nominal value based on overall chemistry. This disadvantage can be overcome by obtaining the Bilger mixture fraction Z by post-processing the species data. Its definition was recently generalized to a general class of fuels and oxidizers [54]. Z is computed from the instantaneous compositions along the flamelet. It is a nonlinear function of $\mathcal{Z}$, as shown in Fig. 3. As a consequence of this, it is recommended to compute the most reactive mixture fraction Z_{mr}, introduced in Section 4.1, using the Bilger mixture fraction definition, when making a comparison with the stoichiometric value Z_{st}.

Similarly, in our formulation, the progress variable C has a different diffusivity than oxygen, despite sharing the same chemical source term. As a result, its profile initially matches the oxygen-based definition in Eq. (5), but diverges at steady state due to the usage of a different diffusion coefficient.

Fig. 4 presents transient temperature profiles over time as a function of the Bilger mixture fraction. The final peak temperature in the steady-state profile aligns closely with the stoichiometric value listed in Table 6. During the transient evolution, the peak temperature initially shifts towards richer conditions before gradually returning towards the stoichiometric location.

The effect of using the real fluid equation of state can be seen from the profile of the compressibility factor, displayed in Fig. 5. The mixture fraction range where effects are seen is larger in the cold initial mixing state than in the hot final steady state. For the DF cases, a small shift to the right is seen in the mixture fraction where the effects appear, compared to the SF case. These effects correspond to the presence of the two-phase region, shown in Fig. 8.

4.2.2. Manifold construction and use

The properties of the transient flamelet evolution, including the source term of progress variable, are tabulated as functions of $\mathcal{Z}$ and C. Contour plots of the source term of C on the manifold are shown in Fig. 6. The evolution of temperature in time shown in Fig. 4, can be understood from the contour plot of the source term. The most rapid evolution occurs in a band slightly towards the rich side of stoichiometry and a second weaker band around $\mathcal{Z} = 0.2$. This structure is present in all three cases.

4.2.3. Combustion modes and multiphase structure

The composition in the flame-generated manifold and therefore the combustion modes defined in Table 2—depend solely on the mixture fraction $\mathcal{Z}$ and the progress variable C. Fig. 7 shows the distribution of the modes in the composition space. All five modes are present. The LTC mode marks the location of the first temperature increase observed in the transient evolution in Fig. 4.

Two very small blue areas, respectively, in the lower left corner and at the upper end of the boundary between pre-HTC and HTC pre-ign. correspond to the exceptional cases not covered by the mode definitions, discussed in Section 2.4.

Combining Figs. 6 and 7 it becomes clear that the source term reaches high values when significant oxygen consumption has already occurred and the flame has reached the HTC region. The different size and shape of the HTC region between, on the one hand, the SF case and, on the other hand, the DF cases, results from the overall higher value of OH concentration at the threshold temperature 1150 K in the SF case.

Combining the information on the transient evolution as shown in Fig. 4 with the location of modes, the type of mode and residence time in a certain mode in the laminar flame can be identified. This time information is not transferred to the turbulent flame calculation. Instead, in the turbulent flame where the tabulated chemistry is used, the evolution of the mixture fraction and the progress variable source term determine the evolution of states.

The full thermochemical state also includes the location of the two-phase region. Fig. 8 shows that this region is triangular in shape. It is bounded by the mixing line $C = 0$, the final steady-state solution, and the line where the liquid volume fraction goes to zero (completeness of the phase transition). This implies that the effects of the multiphase phenomena in the transcritical flame are present only under very rich conditions with $\mathcal{Z} > 0.35$.

Compared with Fig. 7, it is clear that the vapor phase in the two-phase region belongs to the LTC-late combustion mode. Indeed, in the flamelet calculation, the same set of transport equations is solved independently of the thermodynamic state. The local phenomena are determined by the combined effect of thermodynamics (the equations of state and the phase-splitting algorithm), diffusive flux, and chemical reactions. In this way, local states with both a positive liquid volume fraction and a positive progress variable can be generated.

Apart from the time evolution of the complete flamelet profile, shown in Fig. 4, the time delay of reaction progress, between locations with different values of the mixture fraction, is also of interest. Fig. 9, inspired by Fig. 6 in Ref. [38], shows the time evolution of mass

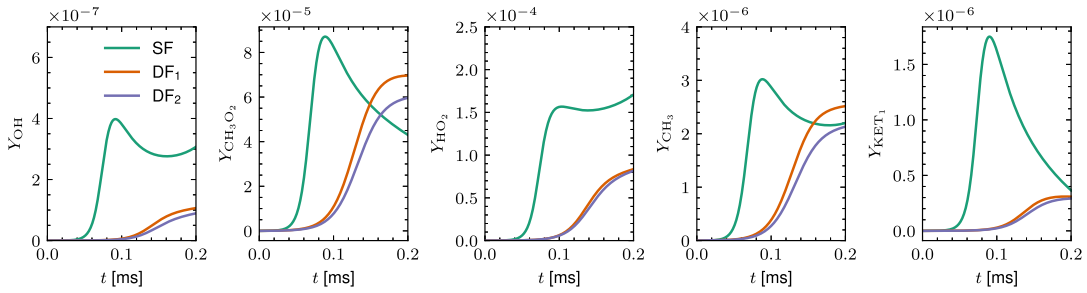

Fig. 2. Temporal evolution of species mass fractions contributing to KET_1 formation in a 0D reactor during n-dodecane stoichiometric combustion with single-fuel (SF) and dual-fuel (DF) with CH_4 or CH_4/C_2H_6 oxidizers at initial temperature of 1000 K.

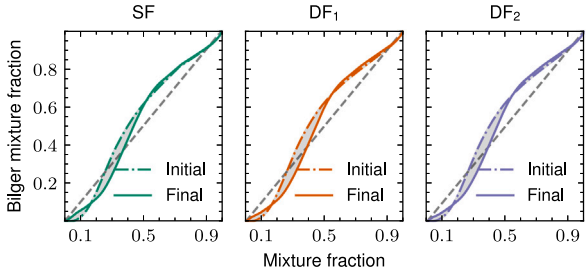

Fig. 3. Relation between mixture fraction from Bilger's definition [54] and from Eq. (9) during the unsteady transcritical flamelet calculation. The shaded region illustrates the temporal variations from the initial to the final states.

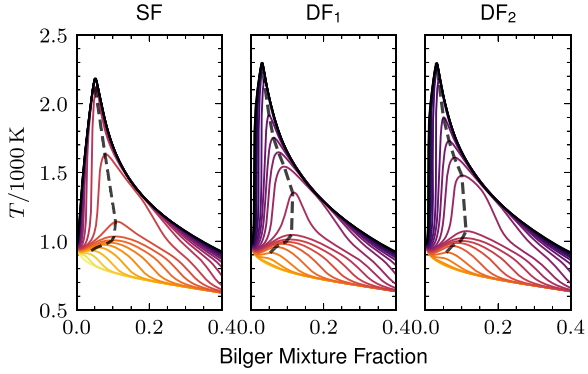

Fig. 4. Temporal variation of the temperature profile as a function of Bilger mixture fraction from the unsteady transcritical flamelet calculation. The dashed line connects the extreme points. Solid lines of the same color represent transient profiles at the same time. (For interpretation of the references to color in this figure legend, the reader is referred to the web version of this article.)

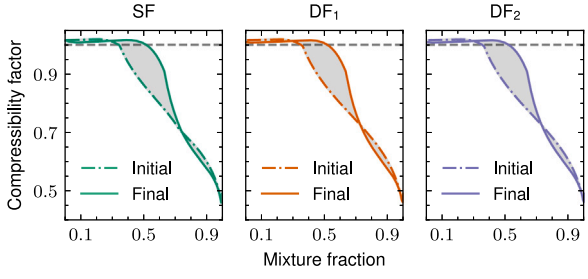

Fig. 5. Compressibility factor as a function of the mixture fraction in the unsteady transcritical flamelet. The shaded region illustrates the temporal variations from the initial to the final states.

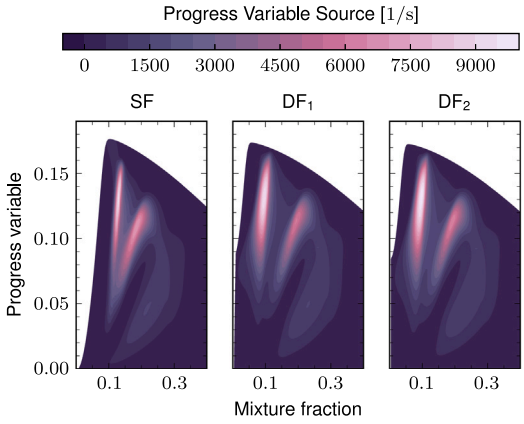

Fig. 6. Progress variable source term as a function of the mixture fraction and unscaled progress variable generated based on the transient counterflow model.

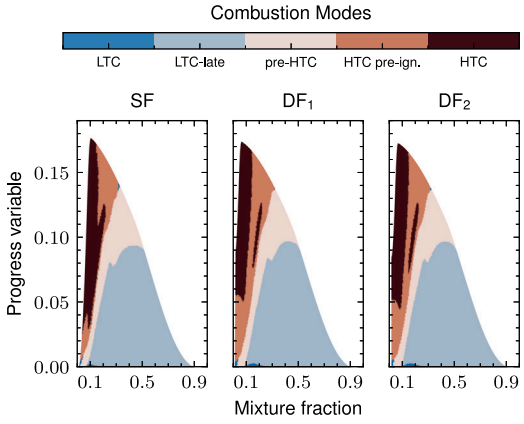

Fig. 7. Combustion modes in mixture fraction and unscaled progress variable space based on the transient counterflow results.

fraction of KET_1 and CO at four values of mixture fraction. Over time, the location of start of combustion in LTC mode, as signaled by the value of KET_1, moves to the richer side, and the sharpness of the rise (and decrease) weakens. At $\mathcal{Z} = 0.7$, inside the two-phase zone, the rate of change is significantly slower, but the peak level of KET_1 is comparable to that in the near stoichiometric zones. On the other hand, the rise of CO, a typical product of incomplete combustion in rich mixtures, develops slower. The fact that certain compositions are reached in a transient flamelet evolution does not imply that these compositions will be accessed in the turbulent flame. In fact, in a jet flame, the very rich zone is present only in the core of the jet and is shrinking. Too little time might be available to reach the concentration

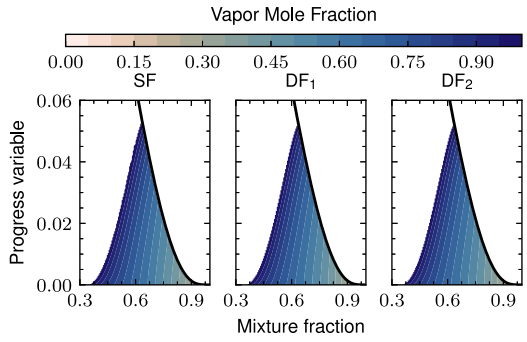

Fig. 8. Variation of the vapor mole fraction in the two-phase region in mixture fraction and progress variable space.

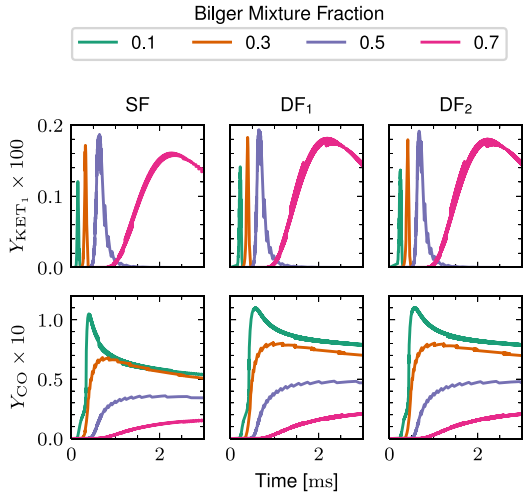

Fig. 9. Evolution of the value of (a) KET_1 and (b) CO at locations with different value of Bilger mixture fraction in the transient flamelet.

values reached in the CDF. This is analyzed further in the next Section when discussing the 3D LES results.

4.3. Turbulent reacting multiphase flow simulation

To simulate the turbulent flame, LES of the transport equations is combined with the reduced chemistry description provided by the CDF-based FGM constructed and analyzed in Section 4.2. Here, we first specify the LES configuration (setup and numerical schemes) and then present the results.

4.3.1. LES configuration

The computational setup and numerical algorithms have been described by Fathi et al. [12], Section 4. The simulations have been carried out using a multi-block structured grid generated in a rectangular cubic domain with a size of $84 \times 42 \times 42$ mm. We apply static zonal mesh refinement. The resulting multi-block structured grid comprises 2864 blocks and 12.7×10^6 cells distributed in seven resolution levels. Approximately 40% of the cells are used for the finest level, with $\Delta y_{\min} = \Delta z_{\min} \simeq 10.25\,\mu$m and $\Delta x_{\min} = 2\Delta y_{\min}$ near the nozzle region, x being the axial direction.

The boundary conditions and numerical schemes used in LES are listed in Table 7. The coupling to FGM is by lookup and linear interpolation in a table containing data on a 256×1024 uniformly spaced mesh for the mixture fraction and the normalized progress variable.

The complexity of LES-MT modeling can significantly increase local computational costs, leading to workload imbalance in traditional domain decomposition. Therefore, dynamic load-balancing strategies [55] are essential to preserve parallel scalability in simulations involving detailed spray flame modeling.

Table 7
Summary of boundary conditions and numerical schemes employed in LES (details and references in Fathi et al. [12]).

Boundary conditions:	
Inflow	Transient velocity profile with no turbulent fluctuations; See Table 5 for others
Outflow	Static pressure = 60 bar; Neumann condition for others
Other	Adiabatic no-slip condition
Numerical schemes:	
Spatial	Conservative; viscous: 2nd-order central; inviscid: ALDM; limiter: van Albada
Temporal	Strang splitting; C-source: 6th-order RK; advection/diffusion: explicit 3rd-order SSP; Δt dynamically adjusted (CFL = 1)

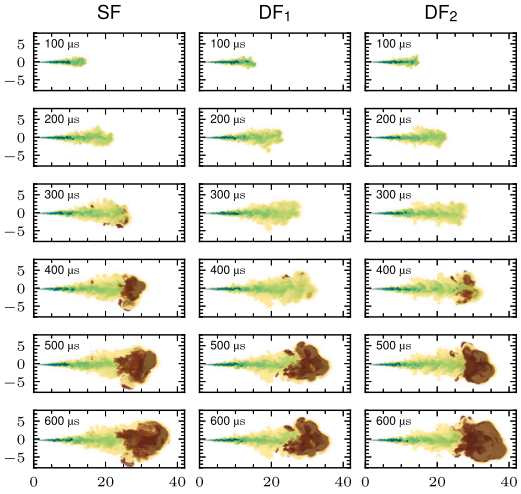

Fig. 10. Temporal snapshots of the turbulent transcritical flame development. The mixturen fraction, shown in light background contours shows the jet contours. The green contours represent the liquid volume fraction in the two-phase region. The dark red area indicates the temperature isosurface at 1800 K. (For interpretation of the references to color in this figure legend, the reader is referred to the web version of this article.)

Table 8
Ignition delay times (in ms) for single and dual fuel cases.

	SF	DF_1	DF_2
This work	0.28	0.38	0.33
Tekgül et al. [41]	0.17	0.31	–
Karimkashi et al. [2]	–	0.31	–
Experiment (OH*) [56]	0.25	–	–

4.3.2. Overall flame development

The development of the jet flame in the three cases is shown in Fig. 10. For each of the three cases, a video of the development is provided as supplemental material. The mixing between fuel jet and ambient oxidizer is visualized by the mixture fraction. In the region close to the injector jet, the two-phase region (TR) is rapidly evolving as seen from the values of the liquid volume fraction. The high temperature isosurface at 1800 K, observed at the tip, shows the zone of fully developed combustion.

The dual fuel cases take more time to reach full development, in agreement with the larger ignition delay time as reported in Table 8 and discussed in Section 4.3.3.

Fig. 11 presents the temporal evolution of the liquid penetration length (LPL) and the vapor penetration length (VPL) for the present

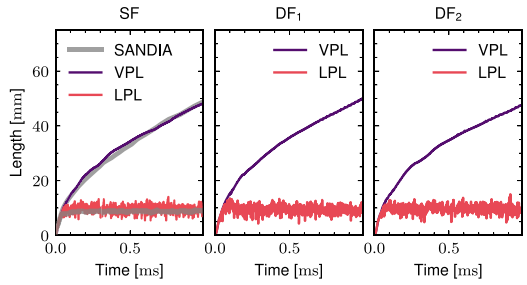

Fig. 11. Comparison between experiments at Sandia [57] and current LES for the vapor penetration length (VPL) and liquid penetration length (LPL) for all cases. The line thickness expresses the uncertainty of the measurements.

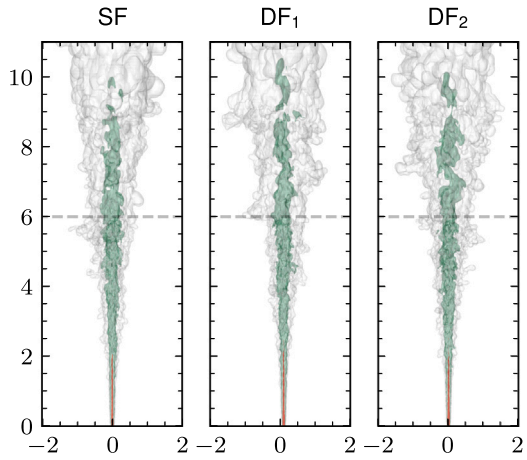

Fig. 12. Snapshot of the flow close to the injector. The liquid region and the two-phase region are highlighted in red and green. Contours of temperature and mass fraction of selected species at the height $x = 6\,\mathrm{mm}$, indicated by the dashed line, are given in Fig. 21. (For interpretation of the references to color in this figure legend, the reader is referred to the web version of this article.)

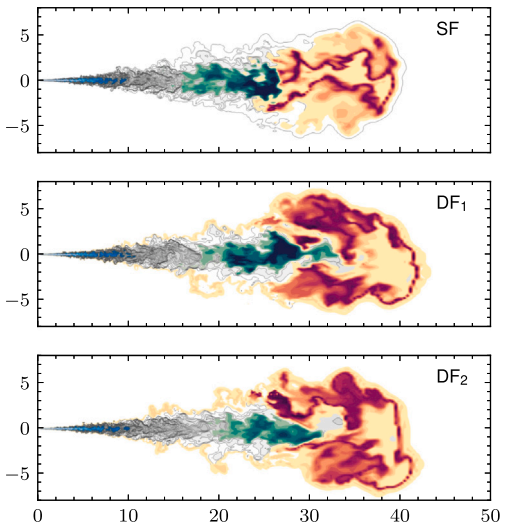

Fig. 13. Comparison of two-phase region (in blue), hot and cold flame regions marked by OH (in red) and CH_2O (in green) distribution for different fuels at 700 µs after the fuel injection. (For interpretation of the references to color in this figure legend, the reader is referred to the web version of this article.)

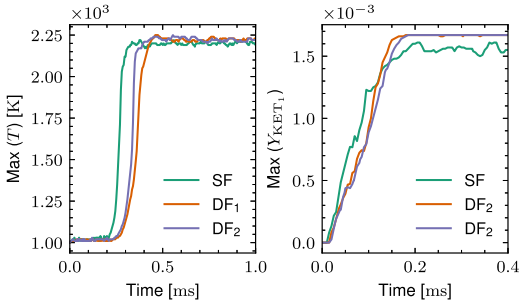

Fig. 14. Temporal evolution of maximum temperature and maximal KET_1 mass fraction observed in the 3D LES.

simulations and experimental measurements for the SF case [57]. For our LES, LPL and VPL are defined as the maximum axial positions where the liquid volume fraction (LVF) is 5% and the mixture fraction is 1%, respectively. The results demonstrate excellent agreement between the LES and the experimental data for both LPL and VPL and low sensitivity to the change in ambient composition.

Fig. 12 shows a snapshot of the liquid region and the TR at times after the liquid region has reached its maximal length. The difference in structure between the three cases is due to statistical variation, rather than to property effects.

Fig. 13 shows the jet flame structure at 700 µs, which highlights the locations of fully developed low-temperature combustion, marked by CH_2O, and high-temperature combustion, marked by OH. The hot flame extends wider in the radial direction because of the presence of a second fuel in the ambient environment.

The overall flame development observed for the case DF_1 is in complete agreement with the previous studies reported in Refs. [2,36,38,41,42]. The start of flame development in the two-phase region is analyzed in Section 4.3.6.

4.3.3. Ignition

In the literature, different characteristic markers have been introduced for the ignition of LTC and HTC. Here we use the mass fraction Y_{KET_1} as marker of LTC and temperature as marker of HTC. Fig. 14 shows the temporal evolution of the maximal values of these markers reached in the 3D turbulent flame. It should be mentioned that the temperature values in LES can slightly differ from temperature values retrieved from the lookup table because they are obtained from the energy equation, including effects of compressibility.

The IDT is defined as time at which the rate of maximal temperature rise is highest. The IDT values obtained in the current work, in two previous modeling studies, and in experiments are listed in Table 8. This longer IDT of the DF cases compared to the SF case, and the slightly lower delay of DF_2 compared to DF_1, were also observed in homogeneous reactor simulations in Section 4.1.

In contrast, the increase of KET_1 starts after a short time of about 0.01 ms related to the n-dodecane chemistry. The peak value of KET_1 increases to levels two orders of magnitude higher than the thresholds defined for LTC and LTC-late, but in agreement with the level reached in location in the counterflow flames shown in Fig. 9. In the DF cases, the rate of increase is slower initially, but eventually overtakes the rate of the SF case, to end at a higher plateau level. This shows the influence of the different composition of the radical pool. The increasing profile shows wiggles possibly caused by the maximum value being found at another location. The plateau level of the DF case is less fluctuation. It could be because the peak is realized in a less turbulent region compared to the SF case as a consequence of the difference in the stoichiometric mixture fraction, but it could also be due to the lower sensitivity of the reactivity to mixture fraction fluctuations.

4.3.4. Combustion modes distribution

At any time, each spatial location in the flame is in a specific combustion mode, depending on the local state of the mixture. Snapshots of the spatial distribution of the modes at different times and for

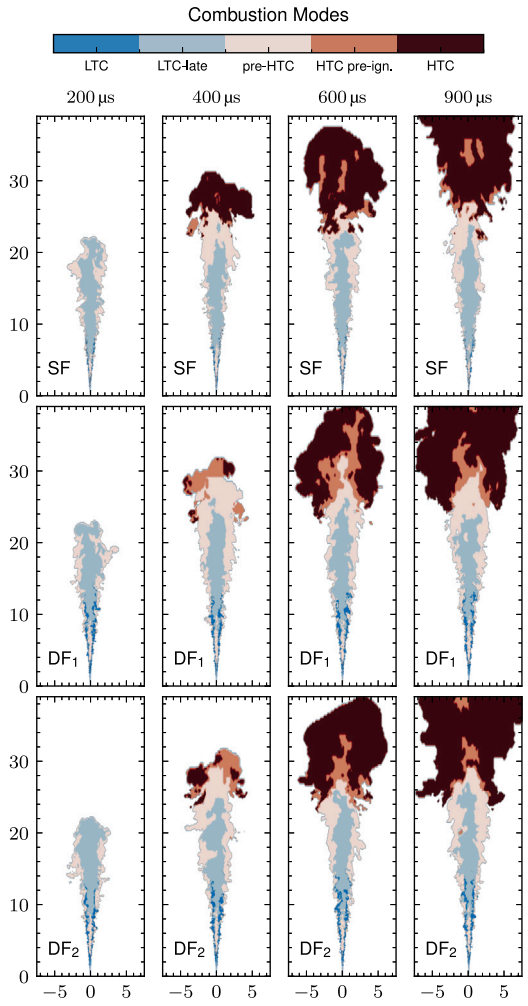

Fig. 15. Contour plots of combustion modes on the z-midplane. From left to right four subsequent times. From top to bottom the three cases.

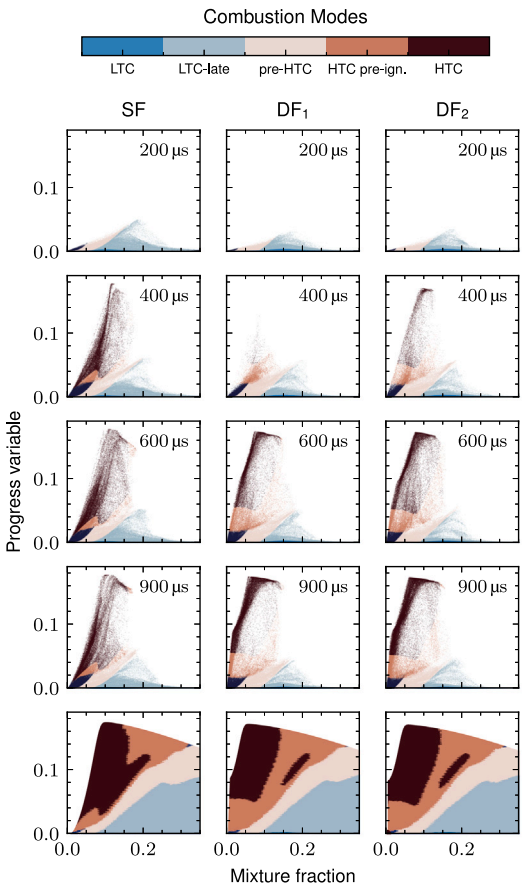

Fig. 16. Scatter plots of accessed combustion modes in the 3D LES. From left to right the three cases. From top to bottom four subsequent times. In the bottom row the modes are given for all states on the manifold.

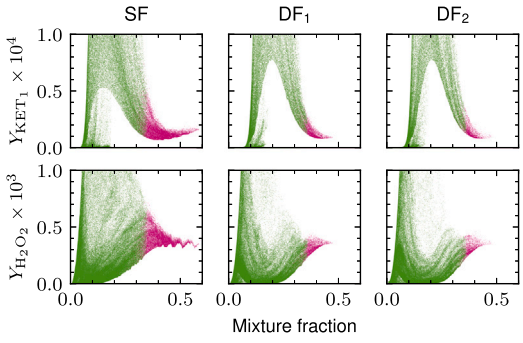

Fig. 17. Scatter plots of low-temperature combustion mode markers KET_1 and H_2O_2 at 900 µs. The magenta color indicates the two-phase region, where the overall mass fraction is shown. (For interpretation of the references to color in this figure legend, the reader is referred to the web version of this article.)

different cases are shown in Fig. 15. On the other hand, at any time a certain region of the manifold is accessed, and in particular a part of each domain associated with a specific mode is accessed. Together, the representations in physical space and composition space provide insight in the progress of ignition and the difference between the different flames.

Fig. 16 shows which combustion modes are accessed in the LES predictions, in the form of a scatter plot in $\mathcal{Z}$-C space with one point per grid cell. From top to bottom, snapshots at different times are shown and from left to right, the three cases. This representation is complementary to the plot of the modes on the complete manifold already displayed in Fig. 7 and here plotted in the last row over the same mixture fraction range as the scatter plots. In the DF_1 case, the signature of HTC ignition is visible in the mode profile and scatter plots at 400 µs. As a consequence of the slightly longer ignition delay time of DF_1 compared to DF_2 (Table 8) the HTC mode is not yet present at this time.

In the scatter plot at 900 µs only states with $\mathcal{Z} < 0.25$ are visible. The TR is outside this range (See Fig. 8). In contrast, in the cross section in Fig. 21 the TR is present. The explanation is that in this region the progress of oxidation is extremely low and $C \approx 0$ and in the scatter plots in $\mathcal{Z}$-C plane the data are not visible. The presence of states in TR can be demonstrated by scatter plots of the combustion mode markers KET_1 and H_2O_2 versus the mixture fraction, shown in Fig. 17. Both species are indeed present in the TR, with KET_1 taking values above and slightly below the threshold value 10^{-5}, respectively, corresponding to states in the LTC-late and pre-HTC mode and H_2O_2 above the threshold value 10^{-4} shared by the LTC-late and pre-HTC mode. The spatial distribution of the marker species in the TR is discussed in 4.3.6.

4.3.5. Heat release rate evolution

Fig. 18 shows the temporal evolution of the volume-integrated HRR for the three cases. The integrated HRR is larger in the DF cases, as a direct result of the second fuel in the ambient environment. The

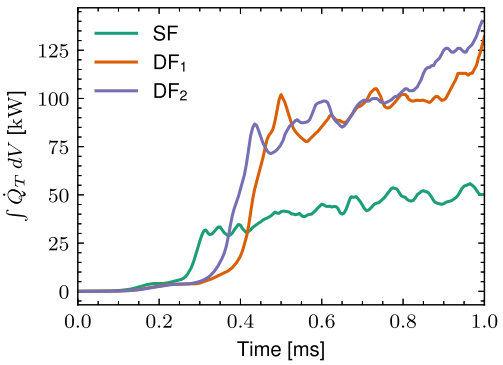

Fig. 18. Temporal evolution of the total heat release rate.

Table 9
Starting time of growth in HRR in each mode (in ms).

Mode	SF	DF_1	DF_2
LTC	0.03	0.03	0.03
LTC-late	0.04	0.06	0.06
pre HTC	0.14	0.16	0.16
HTC pre-ign.	0.25	0.32	0.29
HTC	0.28	0.42	0.35

rise of integrated HRR starts at the IDT reported in Table 8. It can be subdivided in HRR per mode [2,45]. To identify the contributions of the different combustion modes, Fig. 19 shows the temporal evolution of the volume-integrated HRR per mode. As expected, HRR is low in LTC modes and high in HTC mode.

Table 9 lists the times of the first rise in each mode. The difference between the three cases depends on the mode. In LTC mode, HRR starts with a short peak and continues, fluctuating around a plateau value. The LTC-late contribution takes over from LTC immediately after the LTC peak and has a plateau value an order of magnitude higher. Whereas the plateau value in DF-cases in LTC mode three times higher than in the SF case, in LTC mode it is about 10% lower. The pre-HTC mode has a peak at the IDT, given in Table 8. The largest difference between the SF case and the DF cases is observed in the HTC pre-ign. mode because the DF cases reach the threshold temperature value more easily. Also a small difference between the DF_1 and DF_2 cases is observed. They have the same starting time for heat release in LTC modes. But compared to DF_1, DF_2 has an earlier start of HRR in HTC modes and consequently has a lower difference in IDT with the SF case.

4.3.6. Composition of the near field

Close to the injector multiphase phenomena play an important role. Especially in this zone, including the two-phase region, differences arise between the predictions of the multiphase thermodynamics approach used here and other approaches reviewed in Section 2.1. In the previous Sections results on this zone are already included, but were not in focus. In this Section temperature and species profiles in the near field are analyzed.

Fig. 20 shows the mass fraction of n-dodecane in a transverse plane at $x = 6\,\text{mm}$ at $900\,\mu\text{s}$ after fuel injection. From top to bottom: mass fraction in the liquid, in the vapor phase and overall are shown. In both liquid and vapor other species are also present, as already demonstrated for the SF case in Ref. [7] and in agreement with the analysis of the composition space accessed in the flamelet calculations in Section 4.2.

Fig. 21 shows contours of temperature and of mass fraction of KET_1, H_2O_2 and OH in the same domain as Fig. 20. The profiles can be analyzed from the point of view of the combustion modes. Because the temperature is lower than 1150 K, only LTC, LTC-late and pre-HTC modes can be accessed. A clear difference is observed between the composition inside and outside the TR. Inside the TR the temperature and KET_1 are lower than outside, while H_2O_2 is higher than outside. Inside the TR KET_1 is around the threshold value 10^{-5} and H_2O_2 is above the threshold value 10^{-4}, which implies that both the LTC-late and the pre-HTC mode are present. This confirms the conclusions of the analysis of the scatter plots in 17. Outside the TR KET_1 is above the threshold value 10^{-5} and H_2O_2 takes values below and above the threshold 10^{-4}, implying that both the LTC and the LTC-late mode are present. These observations are confirmed by the modes visible in Fig. 15 at height 6 mm. OH is absent inside the TR, but present outside of it. In the DF cases, encircling the TR, a narrow zone with relatively high OH appears. In the SF case, such zone is absent.

This region of LTC-late mode at the base of the jet is disconnected from the LTC-late mode in the more downstream outer part of the jet, which is developing into the HTC modes in the top of the flame.

Structures qualitatively similar to the ones observed here have been observed earlier in studies using LES, LPT, ideal gas EOS and flamelet methods. Disconnected zones of the LTC marker RO_2, close to the injector and further downstream, are visible in some of the results reported in Fig. 5 of Kahila et al. [45], in a study on the sensitivity of flame development to the quantity and timing of the pilot fuel injection. Bao et al. [38], in their Fig. 11, reported the extent of the LTC region, based on RO_2 as marker, in SF and DF_1 case (at 900 K). It can be seen that at 2 ms the LTC zone for the SF case starts at about 6 mm, while in the DF_1 case (corresponding to their DF_2 case) it starts at about 18 mm. This qualitatively agrees with the lower level of KET_1 outside the TR region observed here for DF_1 compare to SF. The occurrence of OH encircling the two phase region, including sensitivity of the phenomenon to fuel composition, has also been observed by Haspel et al. [50] (their Fig. 15) in a study on spatial development of diesel spray jet flames of OME_3 and OME_4. These examples illustrate the opportunities for further model comparison studies. The comparison made here is based on snapshots. A complete analysis would include statistical analysis.

5. Conclusions

This final section summarizes the key features of the developed model, lists the main results, and discusses future perspectives.

5.1. Model selection and development

The MT approach to transcritical jet flames differs in essential ways from other more common approaches for transcritical spray flames. The standard dispersed multiphase flow solvers based on the LPT method are suitable for dilute mixtures (liquid volume fraction $< 10^{-5}$) and subcritical conditions [14]. An alternative method is the single fluid dense gas (DG) approach, including non-ideal fluid effects, but excluding transcritical phase separation. Ignoring phase separation can result in non-physical or ill-defined states when flows cross metastable boundaries [21]. MT overcomes these limitations employing a consistent multicomponent two-phase model for high-pressure real-fluid flows using cubic EOS and vapor–liquid equilibrium (VLE) calculations. The model can represent multicomponent supercritical states and coexisting multicomponent subcritical two-phase states. It also includes the effect of dissolved ambient gases in the liquid fuel phase, which can become substantial at high pressures. It provides detailed phase information that can be directly linked to experimental measurements. In addition to model formulation, the accuracy and cost of numerical solution methods are also important. In this work, an acceptable computational cost could be reached by using optimized VLE solvers in combination with FGM tabulated chemistry [12]. The flamelet approach is appropriate in the considered transcritical flames because they are in the high Damköhler number regime. It allows incorporating of detailed chemistry needed to describe the ignition processes. As a chemical kinetic scheme, an optimal hybrid chemical mechanism proposed by Lapointe et al. [33], which gives an accurate description of two-stage ignition,

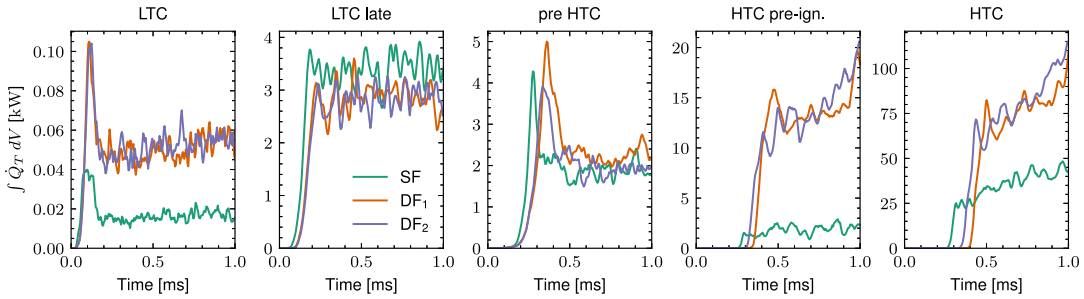

Fig. 19. Temporal evolution of the total heat release rate in different modes of combustion.

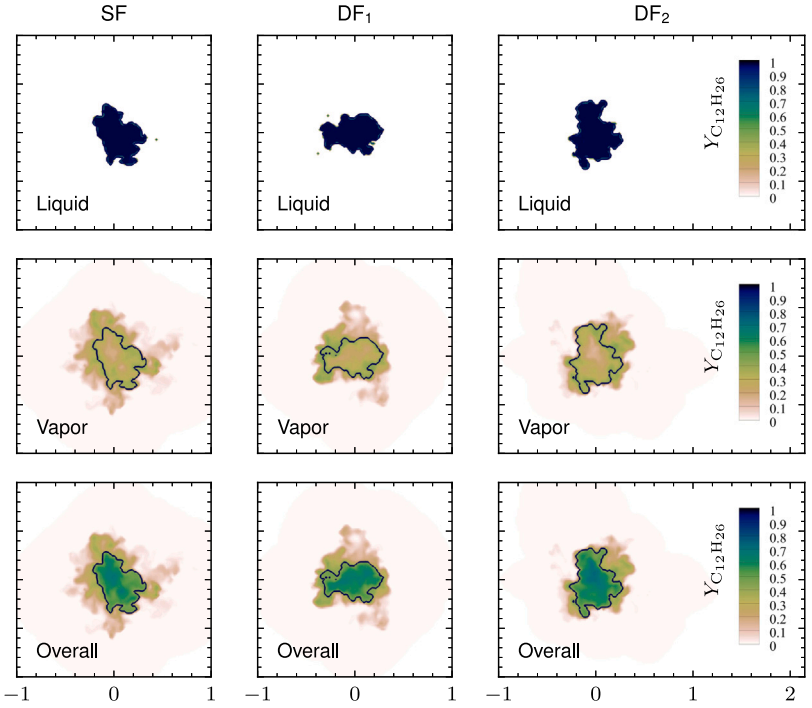

Fig. 20. Contours of n-dodecane mass fraction in a plane at $x = 6$ mm, in a square of 2×2 mm^2 at the jet center, at 900 µs after fuel injection. The solid line highlights the boundary of the two-phase region. From left to right: single fuel (SF), dual fuel with methane in ambient (DF_1) and dual fuel with methane and ethane (DF_2) in the ambient. From top to bottom: Mass fraction in the liquid phase, mass fraction in the vapor or gaseous phase, overall mass fraction.

was used. Analysis of simulations of homogeneous reactors and laminar counterflow flames is an indispensable part of the modeling approach.

Interpretation of computational results requires additional concepts that provide a structure in the detailed flow simulation results. Following the literature [2,45], a set of combustion modes has been defined. They characterize essential steps of the chemical evolution in towards complete combustion. The modes we define are specified in Table 2. The complete development of HTC is possible for a temperature greater than the threshold value of 1150 K where OH is the key species. Below the threshold, in the LTC region, KET_1 and H_2O_2 are selected to characterize the combustion modes. The best interpretation of the results on the mode structure in the flames studied was achieved by combining information contained in profiles in the physical space and in the composition space (the manifold).

5.2. Main results

The LES-MT method essentially differs from the LES-LPT and LES-DG methods in the description of multiphase phenomena in the near field of the jet. Combined with the tabulated chemistry provided by FGM, the possible overlap between the two-phase region and the start of combustion can be studied in detail. The results obtained show that the two-phase region overlaps with the LTC mode of combustion. The chemical breakdown of the fuel and the first formation of key species KET_1 and H_2O_2 is observed in the two-phase region. This first is found in the counterflow diffusion flames used to build the FGM. Next, it is seen that the part of the composition space where overlap occurs is also accessed in turbulent transcritical jet flames.

The LES-MT-FGM simulations, without parameter tuning, accurately predict all major features (LPL, VPL, LOL, IDT) and the development of LTC and HTC regions in good agreement with experiments for the SF case (ECN Spray A). For the dual fuel case DF_1, with methane added in the ambient of the n-dodecane jet, the results agree with previous studies in the literature, but provide a more detailed and accurate description of the near field, the two-phase region.

The flame developments of DF_1 (methane) and DF_2 (methane/ethane) show only a small quantitative difference. This agrees with the fact that the methane number of the secondary fuel of DF_2, the 90:10 by volume mixture of methane and ethane, has a methane number higher than the minimal accepted value for engine applications, mentioned in Section 3.3. The scatter plots of combustion mode shown in Fig. 16, obtained from LES, quantify how the small difference in ignition delay time has an impact on the local flame structure.

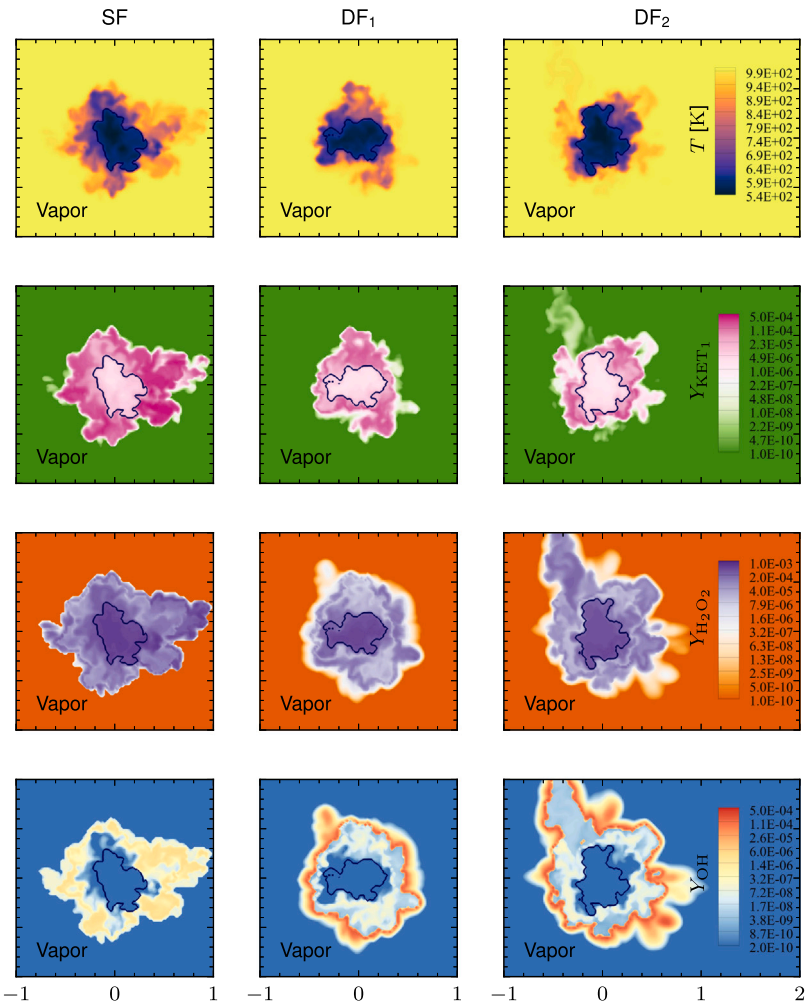

Fig. 21. Contours in plane at $x = 6\,\text{mm}$, in a square of $2 \times 2\ \text{mm}^2$ at the jet center, at $900\,\mu\text{s}$ after fuel injection. The solid line highlights the boundary of the two-phase region. From left to right: single fuel (SF), dual fuel with methane in ambient (DF_1) and dual fuel with methane and ethane (DF_2) in the ambient. From top to bottom contours of temperature and mass fractions of KET_1, H_2O_2, and OH.

5.3. Perspective

The results of this study are based on a specific set of models and submodels all selected with the desire to reach an accurate description. Some model sensitivities deserve further study, for example, the sensitivity of the mode analysis to the chosen threshold values and the impact of variations in strain rate imposed on the flamelet in the FGM approach. The advantages of the Lapointe mechanism compared to other mechanisms used in the literature should be further assessed, focusing on the LTC region and the wider applicability to other fuels.

As mentioned in the Introduction, the dual fuel technique remains valuable while moving away from fossil fuels. Natural gas can be replaced by renewable fuels such as methanol [2], fossil diesel by biodiesel or electrofuels [3]. The method used in this work is very general and in principle can be applied in a straightforward manner to other fuel systems. However, new challenges arise. Thermodynamic data on the fuels (or their surrogate) and an appropriate chemical mechanism must be available. An interesting example is the comparative study of two synthetic fuels, the (poly) oxymethylene ethers OME_3 and OME_4 by Haspel et al. [50], where differences in thermophysical properties, e.g. density and vapor pressure, in inert conditions were found to lead to differences in liquid penetration and mixture formation, and to differences in combustion behavior.

CRediT authorship contribution statement

Mohamad Fathi: Writing – review & editing, Writing – original draft, Software, Methodology, Investigation, Formal analysis, Data curation. **Dirk Roekaerts:** Writing – original draft, Methodology, Investigation, Formal analysis, Conceptualization. **Stefan Hickel:** Writing – review & editing, Software, Resources, Methodology, Investigation, Conceptualization.

Declaration of competing interest

The authors declare that they have no known competing financial interests or personal relationships that could have appeared to influence the work reported in this paper.

Acknowledgments

This work would not have been possible without the computational resources provided by Delft High Performance Computing Center (DHPC) on the DelftBlue supercomputer and by SURF on the Dutch National supercomputer, Snellius.

Appendix A. Supplementary data

Supplementary material related to this article can be found online at https://doi.org/10.1016/j.jaecs.2025.100398.

Data availability

Data will be made available on request.

References

[1] Kahila H, Wehrfritz A, Kaario O, Masouleh MG, Maes N, Somers B, Vuorinen V. Large-eddy simulation on the influence of injection pressure in reacting spray a. Combust Flame 2018;191:142–59. http://dx.doi.org/10.1016/j.combustflame.2018.01.004.

[2] Karimkashi S, Gadalla M, Kannan J, Tekgül B, Kaario O, Vuorinen V. Large-eddy simulation of diesel pilot spray ignition in lean methane-air and methanol-air mixtures at different ambient temperatures. Int J Engine Res 2023;24:965–81. http://dx.doi.org/10.1177/14680874211070368.

[3] Bullermann J, Meyer NC, Krafft A, Wirz F. Comparison of fuel properties of alternative drop-in fuels with standard marine diesel and the effects of their blends. Fuel 2024;357. http://dx.doi.org/10.1016/j.fuel.2023.129937.

[4] Masouleh MG, Wehrfritz A, Kaario O, Kahila H, Vuorinen V. Comparative study on chemical kinetic schemes for dual-fuel combustion of n-dodecane/methane blends. Fuel 2017;191:62–76. http://dx.doi.org/10.1016/j.fuel.2016.10.114.

[5] Dahms RN, Oefelein JC. On the transition between two-phase and single-phase interface dynamics in multicomponent fluids at supercritical pressures. Phys Fluids 2013;25(9):092103. http://dx.doi.org/10.1063/1.4820346.

[6] Matheis J, Hickel S. Multi-component vapor-liquid equilibrium model for LES of high-pressure fuel injection and application to ECN Spray A. Int J Multiphas. Flow 2018;99:294–311. http://dx.doi.org/10.1016/j.ijmultiphaseflow.2017.11.001.

[7] Fathi M, Hickel S, Roekaerts D. Large eddy simulations of reacting and non-reacting transcritical fuel sprays using multiphase thermodynamics. Phys Fluids 2022;34. http://dx.doi.org/10.1063/5.0099154.

[8] Hickel S, Egerer C, Larsson J. Subgrid-scale modeling for implicit large eddy simulation of compressible flows and shock-turbulence interaction. Phys Fluids 2014;26:106101. http://dx.doi.org/10.1063/1.4898641.

[9] Cismondi M, Mollerup J. Development and application of a three-parameter RK-PR equation of state. Fluid Phase Equilibr. 2005;232:74–89. http://dx.doi.org/10.1016/j.fluid.2005.03.020.

[10] Fathi M, Hickel S. Rapid multi-component phase-split calculations using volume functions and reduction methods. AlChE J 2021;67(6):e17174. http://dx.doi.org/10.1002/aic.17174, arXiv:2001.06285.

[11] Fathi M, Roekaerts D, Hickel S. Numerical simulation of transcritical multiphase combustion using real-fluid thermochemical and transport properties. Combust Flame 2025;275:114055. http://dx.doi.org/10.1016/j.combustflame.2025.114055.

[12] Fathi M, Hickel S, Roekaerts D. Large eddy simulations of transcritical e-fuel sprays using real-fluid multiphase flamelet-based modeling. Combust Flame 2025;281:114360. http://dx.doi.org/10.1016/j.combustflame.2025.114360.

[13] Garcia-Villalba M, Colonius T, Desjardins O, Lucas D, Mani A, Marchisio D, Matar OK, Picano F, Zaleski S. Numerical methods for multiphase flows. Int J Multiph Flow 2025;191. http://dx.doi.org/10.1016/j.ijmultiphaseflow.2025.105285.

[14] Jenny P, Roekaerts D, Beishuizen N. Modeling of turbulent dilute spray combustion. Prog Energ Combust 2012;38. http://dx.doi.org/10.1016/j.pecs.2012.07.001.

[15] Subramaniam S. Lagrangian-Eulerian methods for multiphase flows. Prog Energ Combust 2013;39:215–45. http://dx.doi.org/10.1016/j.pecs.2012.10.003.

[16] Ling Y, Zaleski S, Scardovelli R. Multiscale simulation of atomization with small droplets represented by a Lagrangian point-particle model. Int J Multiphas. Flow 2015;76:122–43. http://dx.doi.org/10.1016/j.ijmultiphaseflow.2015.07.002.

[17] Sun Y, Hasse C, Sadiki A. Large eddy simulation based seamless VOF-LPT approach for describing atomization and evaporation processes: Application to jets in crossflow. Int J Heat Mass Transfer 2025;242. http://dx.doi.org/10.1016/j.ijheatmasstransfer.2025.126807.

[18] Yu J, Galindo-Lopez S, Cleary MJ. A coupled Eulerian-Lagrangian approach with explicit volume diffusion subgrid closures for jet breakup and atomisation. Appl Energy Combust Sci 2025;23:100350. http://dx.doi.org/10.1016/j.jaecs.2025.100350.

[19] Wehrfritz A, Vuorinen V, Kaario O, Larmi M. Large eddy simulation of high-velocity fuel sprays: studying mesh resolution and breakup model effects for Spray A. At Spray 2013;23(5):419–42. http://dx.doi.org/10.1615/AtomizSpr.2013007342.

[20] Lacaze G, Misdariis A, Ruiz A, Oefelein JC. Analysis of high-pressure diesel fuel injection processes using les with real-fluid thermodynamics and transport. Proc Combust Inst 2015;35(2):1603–11. http://dx.doi.org/10.1016/j.proci.2014.06.072.

[21] Ma PC, Wu H, Banuti DT, Ihme M. On the numerical behavior of diffuse-interface methods for transcritical real-fluids simulations. Int J Multiphas. Flow 2019;113:231–49. http://dx.doi.org/10.1016/j.ijmultiphaseflow.2019.01.015.

[22] Gaballa H, Habchi C, de Hemptinne JC. Modeling and LES of high-pressure liquid injection under evaporating and non-evaporating conditions by a real fluid model and surface density approach. Int J Multiphas. Flow 2023;160. http://dx.doi.org/10.1016/j.ijmultiphaseflow.2022.104372.

[23] Jafari S, Gaballa H, Habchi C, de Hemptinne JC. Towards understanding the structure of subcritical and transcritical liquid–gas interfaces using a tabulated real fluid modeling approach. Energies 2021;14. http://dx.doi.org/10.3390/en14185621.

[24] Sorrentino G, Ariemma GB, Ferraro F, Fiorina B. Including detailed chemistry features in the modeling of emerging low-temperature reactive flows: A review on the application to diluted and MILD combustion systems. Appl Energy Combust Sci 2024;20. http://dx.doi.org/10.1016/j.jaecs.2024.100291.

[25] Hakim L, Lacaze G, Khalil M, Najm HN, Oefelein JC. Modeling auto-ignition transients in reacting diesel jets. J Eng Gas Turbines Power 2016;138(11):112806. http://dx.doi.org/10.1115/1.4033502.

[26] Wu Z, Rutland CJ, Han Z. Numerical evaluation of the effect of methane number on natural gas and diesel dual-fuel combustion. Int J Engine Res 2019;20:405–23. http://dx.doi.org/10.1177/1468087418758114.

[27] Chung WT, Ma PC, Ihme M. Examination of diesel spray combustion in supercritical ambient fluid using large-eddy simulations. Int J Engine Res 2020;21(1):122–33. http://dx.doi.org/10.1177/1468087419868388.

[28] Ma L, Roekaerts D. Modeling of spray jet flame under MILD condition with non-adiabatic FGM and a new conditional droplet injection model. Combust Flame 2016;165. http://dx.doi.org/10.1016/j.combustflame.2015.12.025.

[29] Bao H, Akargun HY, Roekaerts D, Somers B. The inclusion of scalar dissipation rate in modeling of an n-dodecane spray flame using flamelet generated manifold. Combust Flame 2023;249. http://dx.doi.org/10.1016/j.combustflame.2022.112610.

[30] Hadadpour A, Xu S, Zhang Y, Bai XS, Jangi M. An extended FGM model with transported PDF for LES of spray combustion. Proc Combust Inst 2023;39:4889–98. http://dx.doi.org/10.1016/j.proci.2022.09.014.

[31] Donini A, Bastiaans RJM, van Oijen JA, de Goey LPH. A 5-D implementation of FGM for the large eddy simulation of a stratified swirled flame with heat loss in a gas turbine combustor. Flow, Turbul Combust 2017;98:887–922. http://dx.doi.org/10.1007/s10494-016-9777-7.

[32] Hakim L, Lacaze G, Khalil M, Sargsyan K, Najm H, Oefelein J. Probabilistic parameter estimation in a 2-step chemical kinetics model for n-dodecane jet autoignition. Combust Theor Model 2018;22(3):446–66. http://dx.doi.org/10.1080/13647830.2017.1403653.

[33] Lapointe S, Zhang K, McNenly MJ. Reduced chemical model for low and high-temperature oxidation of fuel blends relevant to internal combustion engines. Proc Combust Inst 2019;37:789–96. http://dx.doi.org/10.1016/j.proci.2018.06.139.

[34] Lin Q, Tay KL, Zhou D, Yang W. Development of a compact and robust polyoxymethylene dimethyl ether 3 reaction mechanism for internal combustion engines. Energ Convers Manag 2019;185:35–43. http://dx.doi.org/10.1016/j.enconman.2019.02.007.

[35] Hadadpour A, Xu S, Pang KM, Bai XS, Jangi M. Effects of pre-injection on ignition, combustion and emissions of spray under engine-like conditions. Combust Flame 2022;241. http://dx.doi.org/10.1016/j.combustflame.2022.112082.

[36] Kahila H, Wehrfritz A, Kaario O, Vuorinen V. Large-eddy simulation of dual-fuel ignition: Diesel spray injection into a lean methane-air mixture. Combust Flame 2019;199:131–51. http://dx.doi.org/10.1016/j.combustflame.2018.10.014.

[37] Moser RD, Haering SW, Yalla GR. Statistical properties of subgrid-scale turbulence models. Annu Rev Fluid Mech 2021;53:255–86. http://dx.doi.org/10.1146/annurev-fluid-060420-023735.

[38] Bao H, Han J, Zhang Y, Di Matteo A, Roekaerts D, Oijen JV, Somers B. Large-eddy simulation of dual-fuel spray ignition at varying levels of methane diluted ambient oxidizer using FGM. Fuel 2023;351. http://dx.doi.org/10.1016/j.fuel.2023.128901.

[39] Yao T, Pei Y, Zhong B-J, Som S, Lu T, Luo KH. A compact skeletal mechanism for n-dodecane with optimized semi-global low-temperature chemistry for diesel engine simulations. Fuel 2017;191:339–49. http://dx.doi.org/10.1016/j.fuel.2016.11.083.

[40] Ranzi E, Frassoldati A, Stagni A, Pelucchi M, Cuoci A, Faravelli T. Reduced kinetic schemes of complex reaction systems: fossil and biomass-derived transportation fuels. Int J Chem Kinet. 2014;46(9):512–42. http://dx.doi.org/10.1002/kin.20867.

[41] Tekgül B, Kahila H, Kaario O, Vuorinen V. Large-eddy simulation of dual-fuel spray ignition at different ambient temperatures. Combust Flame 2020;215:51–65. http://dx.doi.org/10.1016/j.combustflame.2020.01.017.

[42] Wei Y, Zhang Z, Li X, Li G, Zhou M, Belal BY. The ignition characteristics of dual-fuel spray at different ambient methane concentrations under engine-like conditions. Appl Therm Eng 2023;219. http://dx.doi.org/10.1016/j.applthermaleng.2022.119634.

[43] Gadalla M, Karimkashi S, Kabil I, Kaario O, Lu T, Vuorinen V. Embedded direct numerical simulation of ignition kernel evolution and flame initiation in dual-fuel spray assisted combustion. Combust Flame 2024;259. http://dx.doi.org/10.1016/j.combustflame.2023.113172.

[44] Tekgül B, Kahila H, Karimkashi S, Kaario O, Ahmad Z, Lendormy É, Hyvönen J, Vuorinen V. Large-eddy simulation of spray assisted dual-fuel ignition under reactivity-controlled dynamic conditions. Fuel 2021;293. http://dx.doi.org/10.1016/j.fuel.2021.120295.

[45] Kahila H, Kaario O, Ahmad Z, Masouleh MG, Tekgül B, Larmi M, Vuorinen V. A large-eddy simulation study on the influence of diesel pilot spray quantity on methane-air flame initiation. Combust Flame 2019;206:506–21. http://dx.doi.org/10.1016/j.combustflame.2019.05.025.

[46] Fathi M, Hickel S, Roekaerts D. Numerical simulations of real-fluid reacting sprays at transcritical pressures using multiphase thermodynamics. In: Int sem on NICFD prop power. Springer; 2022, p. 169–77. http://dx.doi.org/10.1007/978-3-031-30936-6_17.

[47] Wang J, Carson JK, North MF, Cleland DJ. A new approach to modelling the effective thermal conductivity of heterogeneous materials. Int J Heat Mass Transfer 2006;49:3075–83. http://dx.doi.org/10.1016/j.ijheatmasstransfer.2006.02.007.

[48] Narayanaswamy K, Pepiot P, Pitsch H. A chemical mechanism for low to high temperature oxidation of n-dodecane as a component of transportation fuel surrogates. Combust Flame 2014;161(4):866–84. http://dx.doi.org/10.1016/j.combustflame.2013.10.012.

[49] Kilic AK, Köysüren S, Ong JC, Nemati A, Walther JH. Numerical simulation of a premixed dual-fuel combustion in a constant volume combustion chamber. In: 15th international conference on heat transfer, fluid mechanics and thermodynamics. HEFAT 21, American Society of Thermal and Fluids Engineers; 2021, p. 1628–33.

[50] Haspel P, Gierth S, Popp S, Scholtissek A, Rieß S, Wensing M, Hasse C. Large eddy simulation of OME3 and OME4 spray combustion under heavy-duty conditions. Fuel 2023;353. http://dx.doi.org/10.1016/j.fuel.2023.129097.

[51] Pitsch H, Peters N. A consistent flamelet formulation for non-premixed combustion considering differential diffusion effects. Combust Flame 1998;114(1–2):26–40. http://dx.doi.org/10.1016/s0010-2180(97)00278-2.

[52] Pei Y, Hawkes ER, Bolla M, Kook S, Goldin GM, Yang Y, Pope SB, Som S. An analysis of the structure of an n-dodecane spray flame using tpdf modelling. Combust Flame 2016;168:420–35. http://dx.doi.org/10.1016/j.combustflame.2015.11.034.

[53] Ranzi E, Frassoldati A, Grana R, Cuoci A, Faravelli T, Kelley A, Law C. Hierarchical and comparative kinetic modeling of laminar flame speeds of hydrocarbon and oxygenated fuels. Prog Energ Combust 2012;38(4):468–501. http://dx.doi.org/10.1016/j.pecs.2012.03.004.

[54] Masri AR, Barlow RS. On conserved scalars that preserve stoichiometric mixture fraction. Combust Flame 2024;260. http://dx.doi.org/10.1016/j.combustflame.2023.113224.

[55] van den Oord G, Azizi V, Fathi M, Hickel S. Dynamic multi-level load balancing for scalable simulations of reacting multiphase flows. Int J High Perform Comput Appl 2025;10943420251329199. http://dx.doi.org/10.1177/10943420251329199.

[56] Pastor JV, García-Oliver JM, Micó C, García-Carrero AA. An experimental study with renewable fuels using ECN Spray A and d nozzles. Int J Engine Res 2022;23:1748–59. http://dx.doi.org/10.1177/14680874211031200.

[57] Lillo PM, Pickett LM, Persson H, Andersson O, Kook S. Diesel spray ignition detection and spatial/temporal correction. SAE Int J Engines 2012;5(3):1330–46. http://dx.doi.org/10.4271/2012-01-1239.